

Department of Physics and Astronomy
University of Heidelberg

Master thesis in Physics
submitted by

Nico Schwersenz

born in Mosbach (Germany)

2022

Quantum Dark Matter
in
Reduced Dimensions

This Master thesis has been carried out by Nico Schwersenz
at the Institute for Theoretical Physics
under the supervision of

Prof. Dr. Luca Amendola
and
Prof. Dr. Sandro Wimberger

Zusammenfassung

Quantum Dark Matter (oder Fuzzy Dark Matter, FDM) besteht aus Teilchen mit einer Masse von $m \approx 10^{-22}$ eV. Diese bilden ein Bose-Einstein-Kondensat (BEC) auf kosmologischen Skalen mit de Broglie Wellenlängen $\lambda \approx 1$ kpc, daher der Begriff "fuzzy". Verschmiert durch die Heisenbergsche Unschärferelation, vermindert FDM Dichte-Peaks im Kern galaktischer dunkler Materie halos, die in Simulationen klassischer dunkler Materie (CDM) beobachtet werden, aber deren experimentelle Evidenz fehlt. In dieser Thesis, wird die Schrödinger-Poisson-Gleichung auf eindimensionale Modelle reduziert. Einige Aspekte des vollwertigen, dreidimensionalen Modells finden sich wieder, z.B. quasistationäre Zustände, sogenannte "solitary waves". Besonders Augenmerk wird auf die Genauigkeit der resultierenden Zustände gelegt. Unsere numerische Methode wird gegen ein unabhängig entwickeltes Verfahren im Rahmen einer Kollaboration getestet und die Präzision weiter verbessert.

Abstract

Quantum Dark Matter (or Fuzzy Dark Matter, FDM) consists of particles with a mass $m \approx 10^{-22}$ eV. They form a Bose-Einstein condensate (BEC) on cosmic scales with de Broglie wavelengths $\lambda \approx 1$ kpc, therefore the term "fuzzy". Blurred by the uncertainty principle, FDM alleviates cusp cores of galactic Dark Matter halos, which are found in classical Cold Dark Matter (CDM) simulations, but lack experimental evidence. In this thesis, one-dimensional reduction models of the Schrödinger-Poisson equation are considered and some three-dimensional phenomena, like solitary waves, are recovered. Special attention is paid to the accuracy of resulting states. Our numerical scheme is tested to the independently developed method of our collaborators and its precision is increased further.

Contents

1	Introduction	6
2	Theoretical background	8
2.1	$(3 + 1)D$ Schrödinger-Poisson Equation	8
2.2	Inequivalence between the Quantum-Mechanical and the Hydrodynamic Picture	9
2.2.1	SP \rightarrow Hydro	9
2.2.2	Hydro \rightarrow SP	10
2.3	Dimensionless units	10
2.4	Boundary Conditions	11
2.5	Dimension reduction	12
2.5.1	Homogeneous Matter Sheets – $(1 + 1)$ -SP	12
2.5.2	Strong Confinement–PLAM	12
2.6	Comparison of Interaction Kernels	14
2.7	Governing Equations	15
3	Cosmology	17
3.1	Scale Factor	17
3.2	Initial State	18
3.2.1	Density Contrast δ	18
3.2.2	Phase S	19
3.2.3	Single Realization	20
3.2.4	Exemplary Initial States	20
4	Numerics	22
4.1	Overview of Existing Codes	22
4.2	Time discretization	22
4.3	Spatial discretization	23
4.3.1	Fourier basis	23
4.3.2	B-Spline basis	24
5	Convergence	26
5.1	Convergence Plateau	26
5.2	Linear Theory	29
5.3	Performance	31
6	Asymptotic Dynamics	33
6.1	Construction of ground states	33
6.2	Inelastic Collisions	34
6.3	Dynamical Attractors	38

7	Code optimization	41
7.1	Improve spatial discretization with B-Splines	41
7.1.1	Direct Comparison in x -space	41
7.1.2	Power Spectra	42
7.2	Enhance time stepping	45
7.2.1	4th-order integrator	45
7.2.2	Adaptive Step Size	46
7.3	Conserved Quantities	49
7.3.1	Conservation of Mass	49
7.3.2	Conservation of Momentum	50
8	Conclusion and Outlook	53
8.1	Summary	53
8.2	Future Extension	54
I	Appendix	56
A	Additional Figures	57
B	Lists	63
B.1	List of Figures	63
B.2	List of Tables	67
C	Bibliography	68

1 Introduction

Let us start with a bit of history about Dark Matter and present some evidence for it following [Goetz \[2015\]](#). Dark Matter was first considered in the first half of the 20th century, when the velocity of galaxies belonging to the Coma cluster were measured. The gravitational pull exerted by the luminous matter was just too small to explain the rapidly moving galaxies, which should have long detached and slung out into space. That was when Dark Matter was introduced. Matter, which is invisible, because it only interacts gravitationally.

Since then, several studies supported the existence of Dark Matter. The current amount of large scale structure can not be explained by the baryonic matter only: The gravitational collapse would have taken much longer. By far the most vivid evidence is gravitational lensing ([Bartelmann \[2010\]](#)). Clusters of galaxies bend light rays and appear as giant lenses. Conclusions on the total (visible + invisible) mass can then be made based on the strength of this effect. Another well-observed fact are flat rotation curves of disc galaxies. From the visible mass a strong decline of the rotation velocity with the distance from the galactic center is expected. Instead, the rotation speed is approximately constant with radius. The widely accepted solution to this problem is that the entire galaxy is embedded in a Dark Matter halo ([Amendola \[2022\]](#)), which reinforces the gravitational pull far from the galactic center.

Until now we do not know if the source of the observed effects of localized, additional curvature in space-time. Therefore multiple interpretations are possible. One claims that our theory of gravitation is, at least on large scales, incorrect. The most popular modification is Modified Newtonian Dynamics (MOND). While this model can be considered an add-on ([de Almeida et al. \[2018\]](#)), it has been mostly ruled out as the sole explanation to the discrepancies. Peaks in the angular powerspectrum of CMB anisotropies go against that. The theory, which agrees best with observations, assumes General Relativity is correct. Additional curvature effects are then justified by either anomalous geometric effects of the universe itself, which are hard to prove, or by some kind of Dark Matter.

The most promising theory postulates a Dark Matter particle within the framework of the Λ CDM standard cosmology ([Turner \[2021\]](#)). In Λ CDM visible matter makes up only 5% of the total energy density. All matter, the CDM in Λ CDM, including Cold Dark Matter amount to 30% and is supposed to move at non-relativistic speeds, therefore the term "cold", which leaves 70% to the Λ , which is referred to as the cosmological constant, whose origin also is yet unknown.

The postulation of a Dark Matter particle has an interesting effect. It brings the largest scales together with the smallest scales—cosmology and particle physics. Many candidates for the Dark Matter particle have been put forward. Some of the heavier ones exert the so called cusp-core problem. Motivated by numerical simulation, these heavy particles are destined to form spiky densities in the center of halos, which disagree

with the observed smooth cores. An ultralight particle on the other hand does not have this problem, because its de Broglie wavelength is on the cosmic scale. Roughly speaking, the uncertainty principle forbids infinite clumping and counteracts with the so called "quantum pressure". Motivated by string theory a particle comes into play with a rest mass of $m = 10^{-22}$ eV—the discussion about its mass is not settled yet (Roussy et al. [2021], Rogers and Peiris [2021]) and there are contradicting findings—its wavelength is in the kiloparsec range, the typical size of halo cores.

Numerically there are many options for the implementation of Dark Matter simulations. Compared to direct N -body simulations, that update the position and velocity of each particle per time step and is of $\mathcal{O}(N^2)$ complexity, methods based on the mean-field approach where a single function contains all information about the time development are of $\mathcal{O}(N \log N)$ and therefore much more efficient. The latter have gained attention lately. Partly because they inherently do not have the problem of cusp cores (Niemeyer [2020], Del Popolo and Le Delliou [2021]). They are known under a few different names, which include "Scalar Field Dark Matter (ψ DM)", "Bose-Einstein Condensate (BEC) Dark Matter", "Ultralight Axion Dark Matter", or "Fuzzy Dark Matter" (FDM), as they will be mainly called in this work.

This work carries on the bachelor thesis and master thesis of Zimmermann [2019], who did not only do much of the theoretical modeling, but also develop a code to simulate FDM in one dimension. He published two papers, Zimmermann et al. [2019, 2021], with a focus on the possibilities of the code with respect to physically relevant phenomena. The author joined the group in 2020 and was able to be part of the latter publication, where the growth of structures and asymptotic dynamics are discussed. A part of that paper found its way into this work. The rather laissez-faire handling of numerical precision in the cosmology department caused us to follow the mindset of the condensed matter division, where physical quantities are usually measured up to high precision. Some of the new findings presented here are obtained in cooperation with Prof. Dr. Javier Madroñero and Victor Loiza from the University of Valle in Columbia and include an independent test of the numerical scheme. Other results are based on a numerical upgrade following Auzinger et al. [2016a]. The cpu efficiency is considerably increased, allowing future work to step into higher-dimensional territory.

2 Theoretical background

In this chapter we aim to compress the theoretical part of [Zimmermann \[2019\]](#) into a concise version, only keeping information that is necessary for the understanding of this work. In particular, we skip the derivation of the Schrödinger-Poisson equation from the Einstein-Klein-Gordon equation. [Salehian et al. \[2021\]](#) covers that topic. Due to the problem's complexity, that reduction is only possible to some degree. Firstly, we review the $(3 + 1)$ -dimensional Schrödinger-Poisson equation and adapt it to the finite box and periodic boundary conditions. Secondly, two distinct reduction models into one spatial dimension are outlined. Lastly, we restate the equations ready to be solved in the following chapters.

2.1 $(3 + 1)D$ Schrödinger-Poisson Equation

To keep the number of equations at a minimum, we start with the Schrödinger-Poisson equation in three dimensions:

$$\begin{aligned} i\hbar\partial_t\psi + \frac{3}{2}i\hbar\mathcal{H}\psi &= \left(-\frac{\hbar^2}{2ma^2} \Delta + m\Phi \right) \psi \\ \Delta\Phi &= 4\pi Ga^2(|\psi|^2 - \rho_m(t)), \end{aligned} \quad (2.1)$$

where ψ is the complex scalar field of interest, \hbar is the reduced Planck constant, \mathcal{H} is the Hubble constant, m is the boson mass, a is the cosmic scale factor, Φ is the (self-) interaction potential, G is Newton's constant and $\rho_m(t)$ is the mean dark matter density

$$\rho_m(t) = \frac{1}{|\Omega|} \int_{\Omega} d^3x |\psi(x, t)|^2 \quad (2.2)$$

inside the domain $\Omega = \Omega_1 \times \Omega_2 \times \Omega_3 \subset \mathbb{R}^3$ with side lengths $\Omega_i \subset [0, L_i]$. The Hubble expansion dilutes the total energy $\hat{H}(t)\psi = \left(-\frac{\hbar^2}{2ma^2} \Delta + m\Phi \right) \psi$ in Eq. (2.1) due to its imaginary prefactor. Moving from the proper coordinate system to a comoving one, $\psi \rightarrow a^{-3/2}\psi$, eliminates this term. The mean density becomes time independent and a hermitian, energy conserving, Hamiltonian is left:

$$\begin{aligned} i\hbar\partial_t\psi &= \left(-\frac{\hbar^2}{2ma^2} \Delta + m\Phi \right) \psi \\ \Delta\Phi &= 4\pi Ga^2(|\psi|^2 - \rho_m). \end{aligned} \quad (2.3)$$

It is apparent that only deviations from the mean density, which will be called $\delta(x, t) := |\psi(x, t)|^2 - \rho_m$, contribute to the potential.

SP	Schrödinger-Poisson
\mathcal{H}	Hubble constant
\mathcal{H}_0	Present-day Hubble constant
\hat{H}	Hamilton operator
\hat{H}_K	Kinetic sub-Hamiltonian
\hat{H}_V	Potential sub-Hamiltonian
$\rho = \psi ^2$	Dark matter/BEC density
$\delta = \rho - 1$	Density fluctuations
L	Box size
$\Omega = [0, L)$	Domain
a	Cosmic scale factor
z	Cosmic redshift
$\Omega_\Lambda = 0.7$	Density parameter of the cosmological constant
Ω_m	Matter density parameter
$\Omega_{m,0} = 0.3$	Present-day matter density parameter

Table 2.1: Variables and abbreviations

2.2 Ineqivalence between the Quantum-Mechanical and the Hydrodynamic Picture

Many codes to solve Eq. (2.3) are based on hydrodynamic- or fluid-solvers. They work great on large scales, but lack interference patterns on scales of the de Broglie wavelength and the expected behaviour of Fuzzy dark matter in solitonic cores is not captured. The following reveals the formal inequivalence between the quantum-mechanical and the hydrodynamic picture ([Wallstrom \[1994\]](#)).

2.2.1 SP \rightarrow Hydro

Let us begin with the direction from the Schrödinger equation to the hydrodynamic equations. In natural units $m = \hbar = 1$, the wave function ψ can be written in the Madelung- or hydrodynamic representation

$$\psi = \sqrt{\rho} \exp(iS), \quad (2.4)$$

with the density ρ and a phase S , which defines the velocity v

$$v = \nabla S. \quad (2.5)$$

Now insert Eq. (2.4) into Eq. 2.11 and divide the remaining prefactor, namely ψ . When real and imaginary parts are separated, one arrives at two coupled nonlinear differential equations, which are valid wherever $\psi \neq 0$. The imaginary part is known as the continuity equation

$$\partial_t \rho + \nabla \cdot (\rho v) = 0 \quad (2.6)$$

and derivation of the real part leads to the Euler equation

$$\partial_t v + (v \cdot \nabla)v = -\nabla(Q + V), \quad (2.7)$$

where the so called quantum pressure Q is

$$Q = -\frac{\Delta\sqrt{\rho}}{2\sqrt{\rho}}, \quad (2.8)$$

which is intrinsic to quantum mechanics, but has to be added by hand in hydrodynamics.

2.2.2 Hydro \rightarrow SP

In the opposite direction, from hydrodynamics to Schrödinger-Poisson, we firstly require the velocity to be a gradient of a globally defined, single-valued function $v = \nabla S$. We have to make sure that S is single valued by a quantization condition

$$\oint_L v dl = 2\pi j, \quad (2.9)$$

where L is any closed loop and j is an integer. Phase jumps of multiples of 2π on nodes are thereby eliminated. Now, to obtain the Schrödinger-Poisson equation substitute $v = \nabla S$ and integrate Eq. (2.7). Set the integration constant to zero, and add the remaining equation to i times the gradient of Eq. (2.6). Multiply by the Madelung ansatz for ψ and identify $\nabla\psi$ with $(\nabla\rho + i\nabla S)\psi$. The result is the Schrödinger equation.

2.3 Dimensionless units

Not only for the numerical part it is comfortable to have an equation in dimensionless units, but also to keep the notation compact in the dimension reduction (Sec. 2.5). We follow previous research for the space and time domain, [Schive et al. \[2014\]](#), [Sousbie and Colombi \[2016\]](#), [Taruya and Colombi \[2017\]](#), normalize ψ and make the potential dimensionless:

$$\begin{aligned} \mathbf{x}' &= \left(\frac{m}{\hbar}\right)^{\frac{1}{2}} \left[\frac{3}{2}\mathcal{H}_0^2\Omega_m\right]^{\frac{1}{4}} \mathbf{x} \\ d\tau &= \frac{1}{a^2} \left[\frac{3}{2}\mathcal{H}_0^2\Omega_m\right]^{\frac{1}{2}} dt \\ \psi'(\mathbf{x}', t') &= \frac{\psi(\mathbf{x}', t')}{\sqrt{\rho_m}} \\ V(\mathbf{x}', t') &= a\frac{m}{\hbar} \left[\frac{3}{2}\mathcal{H}_0^2\Omega_m\right]^{-\frac{1}{2}} \Phi, \end{aligned} \quad (2.10)$$

with the present-day Hubble constant $\mathcal{H}_0 = 68 \text{ Mpc km}^{-1} \text{ s}^{-1}$ and the matter-density parameter $\Omega_m = 0.3$. We drop the primes and denote Dimension-full quantities explicitly by the accompanying units. That brings the Schrödinger-Poisson equation into a form, where the role of the scale factor is obvious:

$$\begin{aligned} i\hbar\partial_t\psi &= \left(-\frac{1}{2}\Delta + a(t)V\right)\psi \\ \Delta\Phi &= |\psi|^2 - 1. \end{aligned} \quad (2.11)$$

a acts as a time-dependent coupling constant of the non-linear potential to the Schrödinger equation.

2.4 Boundary Conditions

On both, ψ and V , periodic boundaries of the 0th and 1st derivative, $j \in \{0, 1\}$, are imposed in all three dimensions $i \in \{1, 2, 3\}$:

$$\begin{aligned} (\partial_{x_i})^j \psi(x_i = 0) &= (\partial_{x_i})^j \psi(x_i = L_i) \\ (\partial_{x_i})^j V(x_i = 0) &= (\partial_{x_i})^j V(x_i = L_i). \end{aligned} \quad (2.12)$$

To make further progress from Eq. (2.11), we need to specify the potential. Poisson's equation is equivalent to a convolution of its source term with Green's function $G(\mathbf{x}, \mathbf{x}')$, which is interpreted as the potential of a point mass $\Delta G(\mathbf{x}, \mathbf{x}_0) = \delta(\mathbf{x}, \mathbf{x}_0)$. In contrast to free space, where the well known $1/r$ -potential is valid [Hunt \[2002\]](#):

$$G_{\Delta_3}^{free}(\mathbf{x}, \mathbf{x}') = -\frac{1}{4\pi|\mathbf{x} - \mathbf{x}'|}, \quad (2.13)$$

the situation is different in our compact and periodic domain. The potential can be expanded in a Fourier series:

$$V(\mathbf{x}) = \frac{1}{L_1 L_2 L_3} \sum_{\mathbf{n}} V_{\mathbf{n}} e^{i\mathbf{k}\mathbf{x}} \quad \text{with} \quad V_{\mathbf{n}} = \int_{\Omega} d^3x' V(\mathbf{x}') e^{-i\mathbf{k}\mathbf{x}'}, \quad (2.14)$$

where $\mathbf{n} \in \mathbb{Z}^3$, $\mathbf{k} \in \mathbb{R}^3$ and $\mathbf{k}_i = \frac{2\pi}{L_i}(\mathbf{n})_i$. Inserting Eq. (2.14) as well as the series of $|\psi|^2 - 1$ into Eq. (2.11) yields the expansion coefficients $V_{\mathbf{n}}$:

$$V_{\mathbf{n}} = \begin{cases} 0 & \|\mathbf{n}\| = 0 \\ -\frac{1}{\mathbf{k}^2} & \text{otherwise.} \end{cases} \quad (2.15)$$

As already stated, the 0-mode does not play a role in V , since only the density fluctuations source the potential. In particular that means for the periodic Green's kernel in Fourier space $G_{\Delta_3}^{\pi}(k = 0) = 0$, which allows us to convolve the total density instead of the fluctuations only:

$$\begin{aligned} V(\mathbf{x}) &= \int_{\Omega} d^3x' G_{\Delta_3}^{\pi}(\mathbf{x}, \mathbf{x}') |\psi(\mathbf{x}')|^2 \quad \text{with} \\ G_{\Delta_3}^{\pi}(\mathbf{x}, \mathbf{x}') &= \frac{1}{L_1 L_2 L_3} \sum_{\|\mathbf{n}\| > 0} \frac{-1}{\mathbf{k}^2} e^{i\mathbf{k}(\mathbf{x} - \mathbf{x}')}. \end{aligned} \quad (2.16)$$

We recognize Eq. (2.16) as a convolution-type integral, where the non-local character of the Poisson equation shines through. Eq. (2.11) recast into a single nonlinear Schrödinger equation reads:

$$i\hbar \partial_t \psi = \left(-\frac{1}{2} \Delta + a(t) (G_{\Delta_3}^{\pi} * |\psi|^2) \right) \psi \quad (2.17)$$

2.5 Dimension reduction

The three dimensional SP equation is rather complicated to solve mainly with respect to its implementation. By the reduction to one dimension the problem's complexity and parameter spaces stay untouched, but the reduced computational cost allows for parameter studies to fully understand the governing dynamics.

A fact, that is a little harder to grasp, is what the convolution-type potential implies. By its nonlocal and nonlinear character, the dimensions are coupled, such that they can not be solved independently and reassembled via the superposition principle. That is also true for the setup of the potential itself. How matter is arranged in the remaining directions dictates the interaction in the dimension of interest. Two models of matter arrangement are discussed below.

2.5.1 Homogeneous Matter Sheets – (1 + 1)-SP

The naive, but also most common approach, to study structure formation employing Fuzzy Dark Matter in a low-dimensional context, is just by neglecting one or two dimensions. That is equivalent to demanding a uniform distribution of matter in those dimensions. To arrive at the evolution equation, set $L_3 = L_2 = 1$ and $(\mathbf{n})_{2,3_i} = 0$ in Eq. (2.16), which conserves the Poisson equation, but the point source potential, i.e. its Green's function changes to

$$G_{\Delta_1}^{\pi}(x, x') = \frac{1}{L} \sum_{n>0} \frac{-1}{k_n^2} e^{ik_n(x-x')} \quad (2.18)$$

The (1 + 1)-dimensional Schrödinger-Poisson equation and its alternative form of the nonlinear Schrödinger equation then read

$$\begin{aligned} i\hbar\partial_t\psi &= \left(-\frac{1}{2}\Delta_1 + a(t)V\right)\psi \quad \text{with} \quad \Delta_1 V = |\psi|^2 - 1 \\ \equiv i\hbar\partial_t\psi &= \left(-\frac{1}{2}\Delta_1 + a(t)(G_{\Delta_1}^{\pi} * |\psi|^2)\right)\psi \end{aligned} \quad (2.19)$$

2.5.2 Strong Confinement – PLAM

A more involved reduction, developed by [Zimmermann \[2019\]](#) is the Periodic Line Adiabatic Model (PLAM), for which the general procedure is described here. Let us define $\mathbf{x}_{\perp} = (x_1, x_2)^T \in \mathbb{R}^2$ and introduce the harmonic confining potential V and its ground state χ_0 :

$$V(x_{\perp}) = \frac{1}{2}x_{\perp}^2, \quad \chi_0 = \frac{1}{\sqrt{\pi}}e^{-\frac{x_{\perp}^2}{2}}. \quad (2.20)$$

Notice that we do not impose periodic boundary conditions in the x_{\perp} -plane. We can therefore not take the same Green's function $G_{\Delta_1}^{\pi}$ as before. We start from the three-dimensional periodic kernel $G_{\Delta_3}^{\pi}$, that [Marshall \[2000\]](#) derived recursively via $G_{\Delta_2}^{\pi}$ and

$G_{\Delta_1}^\pi$:

$$G_{\Delta_1}^\pi = \frac{1}{2}|x_1 - x'_1| - \frac{1}{2} \left[\frac{(x_1 - x'_1)^2}{L_1} + \frac{L_1}{6} \right],$$

$$G_{\Delta_2}^\pi = \frac{1}{L_2} G_{\Delta_1}^\pi + \tag{2.21}$$

$$\frac{1}{4\pi} \sum_{m \in \mathbb{Z}} \log \left(1 - 2e^{\frac{22\pi}{L_2} L_1 \left| m + \frac{x_1 - x'_1}{L_1} \right|} \cos \left[\frac{2\pi}{L_2} (x_2 - x'_2) \right] + e^{-\frac{4\pi}{L_2} L_1 \left| m + \frac{x_1 - x'_1}{L_1} \right|} \right),$$

$$G_{\Delta_3}^\pi = \frac{1}{L_3} G_{\Delta_2}^\pi - \frac{1}{\pi L_3} \sum_{m=1}^{\infty} \left\{ \cos \left(\frac{2\pi m}{L_3} (x_3 - x'_3) \right) \times \sum_{n,l \in \mathbb{Z}} K_0 \left(\frac{2\pi m}{L_3} \sqrt{L_1^2 \left[n + \frac{x_1 - x'_1}{L_1} \right]^2 + L_2^2 \left[l + \frac{x_2 - x'_2}{L_2} \right]^2} \right) \right\}. \tag{2.22}$$

Take the limit $\beta \equiv \frac{|x_i - x'_i|}{L_i} \rightarrow 0, i \in \{1, 2\}$ of an infinitely large box in the x_\perp directions, where the $n = l = 0$ terms dominate:

$$G_{\Delta_3}^{\text{mixed}} = \lim_{\beta \rightarrow 0} G_{\Delta_3}^\pi$$

$$= \frac{1}{2\pi L_3} \log |x_\perp - x'_\perp| - \frac{1}{\pi L_3} \sum_{m=1}^{\infty} \cos \left(\frac{2\pi m}{L_3} (x_3 - x'_3) \right) K_0 \left(\frac{2\pi m}{L_3} |x_\perp - x'_\perp| \right) \tag{2.23}$$

Since the wave function factorizes into $\psi(\mathbf{x}) = \psi_1(x_3) \chi_0^\epsilon(x_\perp)$, the external potential V and the mixed-condition Green's function $G_{\Delta_3}^{\text{mixed}}$ feed into the Hamilton operator as follows:

$$\hat{H} = \hat{H}_{x_3} + \hat{H}_\perp^\epsilon \quad \text{with}$$

$$\hat{H}_{x_3} = -\frac{1}{2} \partial_{x_3}^2 + a(t) \left(G_{\Delta_3}^{\text{mixed}} * |\psi|^2 \right),$$

$$\hat{H}_\perp^\epsilon = \frac{1}{\epsilon^2} \left[-\frac{1}{2} \Delta_\perp + V(\mathbf{x}_\perp) \right] = \frac{1}{\epsilon^2} \hat{H}_\perp, \tag{2.24}$$

with $\mathbf{x}_\perp = \mathbf{x}_\perp / \epsilon$. We can insert the factorized wave function into Eq. (2.17):

$$i\partial_t \psi_3(x_3) = \left[-\frac{1}{2} \partial_x + a(t) \int_{\Omega_3} dx_3 U_{\text{LAM}}^\pi(x_3, x'_3) |\psi_3(x'_3)|^2 \right] \psi_3, \tag{2.25}$$

where the new interaction kernel $U_{\text{LAM}}^\pi(x_3, x'_3)$ is found by using the ground state χ_0^ϵ , though which the confinement in x_\perp enters into x_3 . Integrate over the x_\perp -plane:

$$U_{\text{LAM}}^\pi(x_3, x'_3) = \int_{\mathbb{R}^2} d^2 x_\perp \int_{\mathbb{R}^2} d^2 x'_\perp G_{\Delta_3}^{\text{mixed}} |\chi_0^\epsilon(x_\perp)|^2 |\chi_0^\epsilon(x'_\perp)|^2. \tag{2.26}$$

Gradshteyn and Ryzhik [2007] brought this integral into the more appealing form:

$$U_{\text{LAM}}^\pi(x_3, x'_3) = \frac{1}{L_3} \sum_{|m|>0} \left(-\frac{1}{4\pi} \right) e^{\frac{1}{2} k_m^2 \epsilon^2} E_1 \left(\frac{1}{2} k_m^2 \epsilon^2 \right) e^{ik_m(x_3 - x'_3)}$$

$$= \frac{1}{L_3} \sum_{|m|>0} \left(-\frac{1}{4\pi} \right) \mathbb{U} \left(1, 1, \frac{1}{2} (k_3)_m^2 \epsilon^2 \right) e^{ik_m(x_3 - x'_3)}. \tag{2.27}$$

$E_1(x) = \int_1^\infty dt \frac{e^{-tx}}{t}$ denotes the exponential integral and is best evaluated jointly with the exponential function. \mathcal{U} constitutes the "confluent hypergeometric function of the second kind" for which special algorithms exist. The conjunction U_{LAM}^π is an even function with vanishing DC mode. We are not aware of any differential operator with such a Green's function. Consequently, we can not invert the series in Eq. (2.27) to a closed-form, real-space representation and PLAM can only be represented as a NLSE:

$$i\hbar\partial_t\psi = \left(-\frac{1}{2}\partial_x^2 + a(t)(U_{\text{LAM}}^\pi * |\psi|^2) \right) \psi. \quad (2.28)$$

2.6 Comparison of Interaction Kernels

How each reduction method affects the one-dimensional interaction kernel, which corresponds to the potential of a test particle at $x = 0$, is depicted in Fig. 2.1. All potentials are shown for a periodic box of $L = 100$.

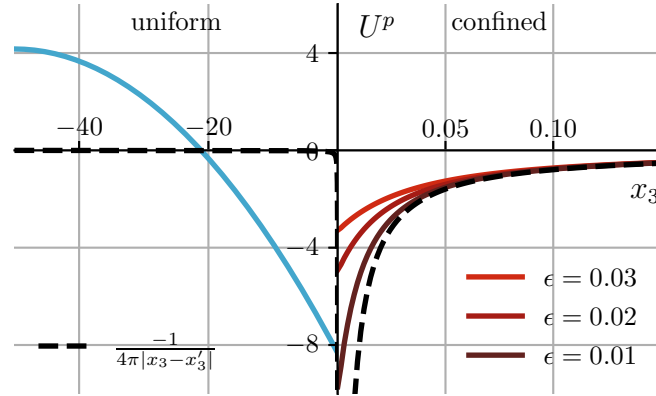


Figure 2.1: Interaction kernels of the two dimension-reduced models. Blue: $(1 + 1)$ -SP; shades of red: PLAM. Mind the different scaling of the x -axis between left and right. As a reference, the same three dimensional kernel is shown in the black, dashed line on both, the left and right side. Figure taken from [Zimmermann et al. \[2021\]](#); copyright: APS

On the left, a uniform matter distribution in $x \perp$ is assumed, the $(1 + 1)$ -SP interaction kernel. For reference, the three-dimensional one ($V \propto 1/r$) is plotted as the black, dashed line. On the right, the PLAM model is shown for three confinement parameters ϵ . Mind the different scaling of the x -axis on the left and right. Due to the vanishing DC-mode, the potential is partially positive.

A key difference lies in the effective interaction range R , which we define as the range, where the gravitational pull is down to a certain percentage α of the maximal value at $x = 0$:

$$\partial_r U^p(R) \equiv \alpha \max |\partial_r U^p| \quad \text{with} \quad 0 < \alpha \ll 1. \quad (2.29)$$

While the gravitational potential under confinement is rather localized with $R \sim \epsilon$ and quickly approaches the desired Newtonian potential (black, dashed line) at large distances $r = |x - x'|$, the effective interaction range for $G_{\Delta_1}^\pi$ scales with the box size

and evaluates to

$$\alpha = \frac{\partial_r G_{\Delta_1}^\pi \big|_{r=R}}{\partial_r G_{\Delta_1}^\pi \big|_{r=0}} = \frac{1/2 - R/L}{1/2}$$

$$\Leftrightarrow R = \frac{L}{2}(1 - \alpha). \quad (2.30)$$

That has consequences on the dynamics and more specifically which states are reached in the asymptotic limit $t \rightarrow \infty$ as discussed in Sec. 6.3.

2.7 Governing Equations

The equation to solve is the one-dimensional Schrödinger-Poisson equation in dimensionless form:

$$i\partial_t \psi(x, t) = \hat{H}(t)\psi(x, t) \quad (2.31)$$

$$= [\hat{H}_K + \hat{H}_V(t)]\psi(x, t)$$

$$= [\partial_x^2 + a(t)V(|\psi(x, t)|^2)]\psi(x, t)$$

$$\partial_x^2 V(|\psi(x, t)|^2) = |\psi(x, t)|^2 - 1 \quad (2.32)$$

$$x \in [0, L)$$

$$\int_0^L |\psi(x, 0)|^2 dx = L, \quad (2.33)$$

where Eq. (2.33) is a relevant constraint, because of the problem's nonlinearity. Changing the normalization does affect the time evolution. V is the non-local, non-linear potential given by the convolution of the density $\delta(x) = |\psi(x)|^2$ with one of the interaction kernels:

$$G(x, x') = \frac{1}{L} \sum_{n>0} \frac{-1}{k^2} e^{ik(x-x')}$$

$$U_{\text{LAM}}^\pi(x, x'; \epsilon) = \frac{1}{L} \sum_{|m|>0} \left(-\frac{1}{4\pi} \right) e^{\frac{1}{2}k_m^2 \epsilon^2} E_1 \left(\frac{1}{2}k_m^2 \epsilon^2 \right) e^{ik_m(x-x')} \quad (2.34)$$

Smooth boundary conditions $\psi(0, t) = \psi(L, t)$, $\partial_x \psi(0, t) = \partial_x \psi(L, t)$ are imposed and naturally fulfilled by the following Fourier basis approach. The scale factor is given by the Friedmann equation in a flat and radiation-free universe, see (Eq. 6.23) in [Ryden \[2003\]](#),

$$\left(\frac{\dot{a}}{a} \right)^2 = \mathcal{H}_0^2 (\Omega_m a^{-3} + \Omega_\Lambda), \quad (2.35)$$

with the present-day Hubble constant $\mathcal{H}_0 = 68 \text{ km s}^{-1} \text{ Mpc}^{-1}$, the present-day matter density parameter $\Omega_{m,0} = 0.3$, which dilutes with the volume of the cosmic expansion and only coincides with Ω_m , because we set $a(t = \text{today}) = 1$, and the density parameter of the cosmological constant $\Omega_{\Lambda,0} = \Omega_\Lambda = 0.7$, staying constant in time. The background cosmology $a(t)$ will be computed in the next chapter.

$(3 + 1)$ -SP has been brought into a comoving form, which follows the expansion of the universe and dimensionless units were introduced to simplify further progress. We saw that the hydronamical and the quantum-mechanical picture differ on nodes of ψ and are not equivalent. The two distinct reduction models into $(1 + 1)$ -SP and PLAM from [Zimmermann \[2019\]](#) were restated and their point-source interactions compared. The governing equations of are ready to be studied. That concludes the theoretical part about FDM.

3 Cosmology

The background cosmology enters the governing Eq. (2.32) in two ways: Firstly, through the scale factor a , which obeys a linear differential equation, and secondly, through the initial state $\psi(x, a_{\text{start}})$, which will be described by statistical variables. Both are separable from the governing equations and therefore discussed here.

3.1 Scale Factor

The basic relation between the redshift z and the scale factor a is:

$$a = \frac{1}{1+z}. \quad (3.1)$$

Let us restate the calculation of the cosmic scale factor $a(t)$ as described in the preceding work [Zimmermann et al. \[2019\]](#). We substitute the Friedmann equation into the dimensionless units and obtain the equation to solve:

$$\begin{aligned} dt &= \frac{1}{\dot{a}a^2} \left[\frac{3}{2} H_0^2 \Omega_{m,0} \right]^{\frac{1}{2}} da \\ &\stackrel{\text{Eq. 2.35}}{=} \left[\frac{3\Omega_{m,0}}{2(\Omega_{m,0}a^{-3} + \Omega_\Lambda)} \right]^{\frac{1}{2}} da. \end{aligned} \quad (3.2)$$

Since there is no closed-form solution for all values of $\Omega_{m,0}$, we perform the integration numerically. First, divide the interval $[a_{\text{ini}}, a_{\text{fin}}]$ into K equidistant parts $\Delta a = \frac{a_{\text{fin}} - a_{\text{ini}}}{K}$ and apply the midpoint method:

$$t(a_k) = t(a_{k-1}) + \left. \frac{dt}{da} \right|_{a_{k-1} + \frac{\Delta a}{2}} \cdot \Delta a, \quad t(a_{\text{ini}}) = 0. \quad (3.3)$$

We store the values $t(a_k)$ in a look-up table and interpolate linearly, if the scale factor at intermediate times is needed. Computationally this amounts to a $\mathcal{O}(1)$ operation. Although we choose $K = 10^5$, which guarantees convergence of the end-result of $\mathcal{O}(10^{-8})$ high precision is not necessary at this point. When sensitive data is compared, e.g. wave functions in Sec. 7.1, we make sure to use the same exact look-up table. In Fig. 3.1 the development of the scale factor with dimensionless time is given. In the flat universe we consider, we have $\Omega_{m,0} + \Omega_\Lambda = 1$. $\Omega_\Lambda = 1$ means no matter is abundant and the evolution is $a \propto \mathcal{H}_0 t$. By adding matter content to the universe, the expansion until today ($a = 1$) is slower. In accordance with the standard Λ CDM model, we choose $\Omega_{m,0} = 0.3$ and accordingly $\Omega_\Lambda = 0.7$ for the our cosmological simulations.

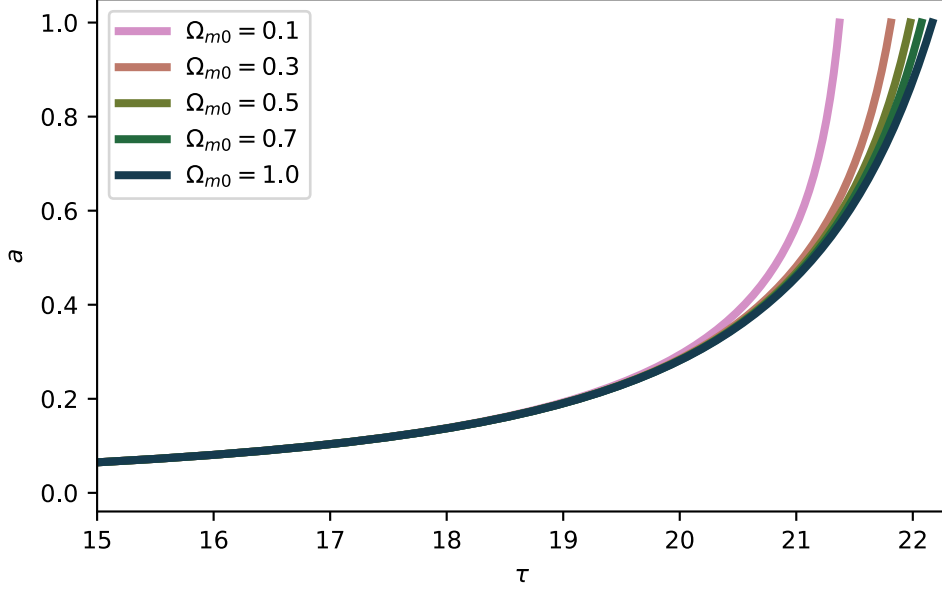


Figure 3.1: Scale factor a as a function of the dimensionless time τ obtained from numerical integration. Small matter density parameters $\Omega_{m,0}$ result in slower growing universes.

3.2 Initial State

At early times the density fluctuations are small and the wave function can be expressed in the Madelung form $\psi(x) = \sqrt{1 + \delta(x)}e^{iS(x)}$. How the density fluctuations and the phase are constructed is depicted schematically in Eq. (3.4) and explained in more detail thereafter.

$$\begin{aligned}
 & \xrightarrow{\text{CAMB}} P_{\text{CDM,lin}}^{\text{3D}}(k, a = 1) \xrightarrow{D(a_{\text{start}})} P_{\text{CDM,lin}}^{\text{3D}}(k, a_{\text{start}}) \xrightarrow{T_{\text{FDM}}} P_{\text{FDM,lin}}^{\text{3D}}(k, a_{\text{start}}) \\
 & \xrightarrow{\sigma^{\text{1D}} \stackrel{!}{=} \sigma^{\text{3D}}} P_{\text{FDM,lin}}^{\text{1D}}(k, a_{\text{start}}) \xrightarrow[\text{Rayleigh}]{\text{Periodicity}} \sigma^2(k, a_{\text{start}}) \xrightarrow{\text{Rayleigh}} |\delta_k(a_{\text{start}})|, \varphi_k(a_{\text{start}}) \\
 & \xrightarrow{\text{Eq. (3.13)}} S_k(a_{\text{start}}) \xrightarrow{\mathcal{F}^{-1}, \text{Madelung}} \psi(x, a_{\text{start}}) \tag{3.4}
 \end{aligned}$$

3.2.1 Density Contrast δ

Similar to Zhang et al. [2019], the first step towards a cosmological Gaussian random field (GRF) is by assuming a homogeneous and isotropic background density $\rho = 1$, which is then superposed with fluctuations. The "Code for Anisotropies in the Microwave Background" (CAMB) takes care of all physics before matter domination and returns the linear, present-day matter power spectrum $P_{\text{CDM,lin}}^{\text{3D}}(k, a = 1)$. Next, project the spectrum to $z = 100$ via the normalized, linear growth function $D(1, a_{\text{start}})$, where this approximation based on the linear perturbation theory holds. The linear growth function $D(a, a_{\text{start}})$ is derived in Sec. 5.2. Apply the empirical transfer function

$$T_{\text{FDM}} = \frac{\cos(x^3)}{1 + x^8} \quad \text{with} \quad x = 1.61 \left(\frac{m}{1 \times 10^{-22} \text{ eV}} \right)^{\frac{1}{18}} \left(\frac{k}{k_{\text{Jeans}}} \right) \tag{3.5}$$

from Zhang et al. [2019], to account for the suppression of high modes of FDM compared to CDM. Demand the same variance of the fluctuations in one and three dimensions:

$$\begin{aligned} (\sigma^{1D})^2 &\stackrel{!}{=} (\sigma^{3D})^2 \\ \Leftrightarrow \frac{1}{2\pi} \int_{\mathbb{R}} dk P^{1D}(k) &= \frac{4\pi}{(2\pi)^3} \int_0^\infty dk P^{3D}(k) k^2 \\ \Leftrightarrow P^{1D}(k) &= \frac{k^2}{2\pi} P^{3D}(k). \end{aligned} \quad (3.6)$$

The last equation holds, because the 1D power spectrum is an even function. By truncation of the domain to a finite size L an additional factor of L^{-2} is introduced, because the integrals in Eq. (3.6) become sums:

$$\frac{1}{2\pi} \int_{\mathbb{R}} dk P(k) \xrightarrow{\text{Periodicity}} \frac{1}{L^2} \sum_k P(k). \quad (3.7)$$

Identify the power spectrum with the ensemble-average density fluctuation in k -space, $P(k) = \frac{1}{L} \langle |\delta_k|^2 \rangle$, and arrive at:

$$\langle |\delta_k|^2 \rangle = L \frac{k^2}{2\pi} D^2(1, a_{\text{start}}) T_{\text{FDM}}^2 P_{\text{CDM, lin}}^{3D} \quad (3.8)$$

δ_k is a complex function, whose real- and imaginary part are statistically independent. Apply the Madelung transform $\delta_k = |\delta_k| e^{i\varphi_k}$. The probability distribution of the length $|\delta_k|$ of the two-dimensional (real- and imaginary part) vector δ_k is a Rayleigh distribution and the phase φ_k is uniform.

$$p(|\delta_k|, \varphi_k) d|\delta_k| d\varphi_k = \frac{|\delta_k|}{\sigma(k)^2} \exp\left(-\frac{|\delta_k|^2}{2\sigma(k)^2}\right) d|\delta_k| d\frac{\varphi_k}{2\pi} \quad (3.9)$$

A relation between $\langle |\delta_k|^2 \rangle$ and σ_k is established by calculation of the variance of Eq. 3.9: $\langle |\delta_k|^2 \rangle = 2\sigma(k)^2$ In total, the variance of the density fluctuations of the one-dimensional FDM matter power spectrum at $a = a_{\text{start}}$ is:

$$\sigma(k)^2 = \frac{L}{2} \frac{k^2}{2\pi} D^2(a_{\text{start}}) T_{\text{FDM}}^2 P_{\text{CDM, lin}}^{3D} \quad (3.10)$$

3.2.2 Phase S

To establish a relation between the fluctuation's phase S and amplitude $|\delta(x)|$, we make use of the linear growth

$$\delta(x, a) = D(a) \delta(x, a_{\text{start}}), \quad (3.11)$$

differentiate with respect to time, combine it with the linearized, one-dimensional continuity equation

$$\partial_t \rho + \frac{1}{a} \partial_x v = 0 \quad (3.12)$$

and express the velocity in terms of $v = \frac{1}{ma} \partial_x S$ to find

$$\partial_x^2 S(x, a_{\text{start}}) = -ma_{\text{start}}^2 \mathcal{H}(a_{\text{start}}) \delta(x, a_{\text{start}}) \quad (3.13)$$

That concludes the discussion about the statistics of GRFs. Left over is the construction of a single realization.

3.2.3 Single Realization

To achieve moduli $|\delta(k)|$ from a Rayleigh distribution

$$f(|\delta(k)|; \sigma) = \frac{|\delta(k)|}{\sigma^2} e^{-\frac{|\delta(k)|^2}{2\sigma^2}}, \quad (3.14)$$

make use of the "inverse transform sampling" or sometimes called "exact inversion". Firstly, draw random numbers u from a uniform distribution $U \sim \text{Unif}(0, 1)$. Solve $F(F^{-1}(u)) = u$ for $F^{-1}(u)$, where F is the cumulative distribution function (cdf):

$$\begin{aligned} F(u; \sigma) &= \int_0^u f(u'; \sigma) du' \\ &= 1 - e^{-\frac{u^2}{2\sigma^2}} \end{aligned} \quad (3.15)$$

and arrive at the Rayleigh distributed moduli

$$|\delta_k| = F^{-1}(u) = \sigma \sqrt{-2 \ln(1 - u)}. \quad (3.16)$$

Lastly, replace $1 - u$ by u , which leads to the same distribution. The construction of random phases φ is rather simple in comparison. Make sure to use a second, statistically independent uniform distribution u :

$$\varphi = 2\pi u. \quad (3.17)$$

Assemble both by the Madelung representation to get δ_k and apply an inverse Fourier transform for the result of the real, discrete coefficient vector $\delta(x)$. For the phase S , solve the Poisson equation, Eq. (3.13), preferably in k -space:

$$S(x, a_{\text{start}}) = \mathcal{F}^{-1} \left[-\frac{1}{k^2} \right] \mathcal{F} C \delta(x, a_{\text{start}}) \quad \text{with} \quad C = -m a_{\text{start}} \mathcal{H}(a_{\text{start}}) \quad (3.18)$$

Assemble $\psi(x, a_{\text{start}})$ again, via the Madelung representation.

3.2.4 Exemplary Initial States

In Fig. 3.2 some exemplary states are shown. In small boxes the state is mostly a single period sine function and their amplitude grows with L . That is no surprise, but rather what we expect, having a correlation length σ inside a box with periodic boundary conditions. Density fluctuations saturate at $\delta \approx 0.15$ for a box $L \approx 1000$. Beyond that size, states only become more oscillatory. Although the amplitude of density fluctuations is bounded, the computational demand rises with the box size, as the total mass accumulates, see Ch. 5

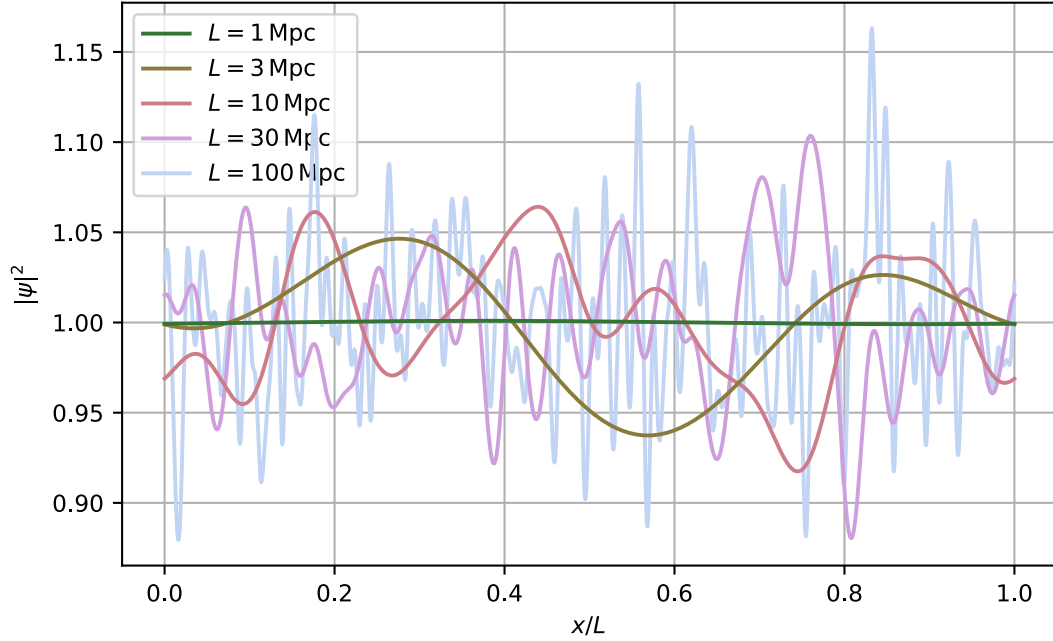


Figure 3.2: Exemplary, rescaled cosmological initial states scaled with the box size L for a better comparison. Dimensionless box sizes $L \in \{48, \dots, 4877\}$ correspond to real distances of $L \in \{1 \text{ Mpc}, \dots, 100 \text{ Mpc}\}$. The finite correlation length σ together with the periodic box suppresses the structure in small boxes. Density fluctuations grow in amplitude and in their number of oscillations as the box size increases. They saturate at $\delta \approx 0.15$.

The the background cosmology is now fixed and stored in a look-up table. Based on statistical quantities, modifications to the three-dimensional power spectrum obtained from CAMB can be applied to set up initial states. What hinders us from propagating $\psi(x, a_{\text{start}})$ in time, is a solution to Eq. (2.32). By now, it might be obvious, that no analytical solution exists to that problem, which is why we turn to a numerical implementation, see the next Ch. 4.

4 Numerics

Before introducing the numerical method, its temporal and spatial discretization, we review the field of preexisting codes and explain, why it is necessary to have yet another one.

4.1 Overview of Existing Codes

There are many existing codes out there to simulate Dark Matter. A recent review is provided by [Zhang et al. \[2019\]](#), which is extended in Tab. 4.1. They fit in one of the two categories: 1) Lagrangian-based solvers develop the density field via the Madelung representation from fluid dynamics. The quantum-mechanical effect of wave interference is absent in this formulation, which disqualifies the entire category for our purposes. 2) Eulerian-based methods solve directly for the wave function in the Schrödinger-Poisson system. Interference patterns inside halo cores are reported, but any of the codes is at least two dimensional—whether they are publicly available is a different story. For our one-dimensional cosmological "toy model", we consequently need a new code.

Cite	Method (Code base)	Dimension	Box size [Mpc]	Resolution	Refinement	Time Step	Open source
Schive et al. [2018a]	GAMER-2	3	14.26	10,240 ³	geometrically similar	optimized adaptive, spatially non-uniform	yes
Li et al. [2019]	SPoS	3	10	1024 ³	-	$\min(\frac{1}{\psi}, \frac{a^2 \Delta t^2}{6})$	no
Mina et al. [2020]	SCALAR(RAMSES)	3	1	64 ³ (256 ³)	cell-by-cell	$\min(\frac{2\pi}{5 V_{\text{max}} }, \frac{\sqrt{3}\Delta t^2}{10})$	not uploaded yet
Teyssier [2002]	RAMSES	3	100	256 ³ (8192 ³)	geometrically similar	CFL, Free-fall, $\dot{a} < c$	yes
Springel et al. [2021]	GADGET-4	3	25	256 ³			
Bryan et al. [2014a]	ENZO	1,2,3	64	128 ³	rectangular		yes

Table 4.1: Existing codes to simulate Dark Matter adapted from [Zhang et al. \[2019\]](#). More recent developments were added. Quantitative features stem from the respective publications. The first half are Schrödinger-Poisson solvers, the second half hydrodynamic solvers.

4.2 Time discretization

We realize that the sub-Hamiltonians \hat{H}_K and \hat{H}_V are exactly solved and efficiently approximated, respectively, and follow the path of operator splitting methods. The splitting method used in our previous work [Zimmermann et al. \[2021\]](#) and partially this work, is the three-stage Strang splitting. It approximates the time evolution of Eq. (2.32) in the following standard symmetrized manner:

$$\hat{U}_{K+V}(t_0, \Delta t) = \hat{U}_K(\frac{\Delta t}{2}) \circ \hat{U}_V(t_0 + \frac{\Delta t}{2}, \Delta t) \circ \hat{U}_K(\frac{\Delta t}{2}) + \mathcal{O}(\Delta t^3) \quad (4.1)$$

\hat{U}_K and \hat{U}_V are the time evolution operators to the kinetic and potential sub-problem. To see that the Strang splitting is equivalent to the exponential of the Hamiltonian up

to second order, we apply the Baker-Campbell-Hausdorff (BCH) formula to the right hand side of Eq. (4.1). Let us define for convenience the exponents of the evolution operators as

$$X := -iaV(|\psi|^2)\Delta t \quad (4.2)$$

$$Y := -i\partial_x^2 \frac{\Delta t}{2}, \quad (4.3)$$

apply the BCH formula twice

$$\exp(Y) \exp(X) \exp(Y) := \exp(Y) \exp(Z(X, Y)) := \exp(\hat{H}'(Y, Z(X, Y))) \quad (4.4)$$

and solve for the operator \hat{H}' , that the Strang splitting represents:

$$\begin{aligned} \hat{H}' &= Y + Z(X, Y) + \frac{1}{2}[Y, Z(X, Y)] \\ &= Y + X + Y + \frac{1}{2}[X, Z(X, Y)] + \frac{1}{2}[Y, X + Y + \frac{1}{2}[X, Y]] + \dots \\ &= Y + X + Y + \frac{1}{2}(XY - YX) + \frac{1}{2}(YX + Y^2 - XY - Y^2) + \mathcal{O}(\Delta t^3) \\ &= X + 2Y + \mathcal{O}(\Delta t^3) \\ &= \hat{H}(t) + \mathcal{O}(\Delta t^3). \end{aligned} \quad (4.5)$$

Terms of $\mathcal{O}(\Delta t^2)$ cancel and H' is indeed second order accurate. In comparison to the first order accurate Lie-Trotter splitting, no additional computation steps are necessary, because consecutive kinetic operators with a time step $\frac{\Delta t}{2}$ can be combined to a single operator with a time step Δt . The only difference is that \hat{U}_V is evaluated at intermediate times $t_0 + \frac{\Delta t}{2}$.

4.3 Spatial discretization

We outline two methods: One uses a pseudospectral decomposition and the other is based on B-Splines. Although we show results for both, only the pseudospectral approach is house-intern. The B-Spline method was developed by the group of Javier Madroñero from the University of Valle in Columbia, which is why we can only state the basic framework and show some end-results. Our cooperation results in an upcoming paper

4.3.1 Fourier basis

We choose an equidistant grid of size N in x -space $x_n = n\Delta x$ and the orthogonal k -space $k_n = \frac{2\pi}{n\Delta x}$, $n \in N$. In contrast to a spectral method, where ψ is decomposed into eigenfunctions, we simply use plain waves. The sub-problems are solved separately and $\mathcal{F}/\mathcal{F}^{-1}$ stands for the Fourier transform and its inverse. In Fourier space the kinetic sub-problem is solved exactly:

$$\begin{aligned} i\partial_t \psi(x_n, t) &= \partial_x^2 \psi(x_n, t) = \mathcal{F}^{-1} \text{diag} \left[\frac{k_n^2}{2} \right] \mathcal{F} \psi(x_n, t) \\ \hat{U}_K(\Delta t) &= \mathcal{F}^{-1} \text{diag} \left[\exp \left\{ -i \frac{k_n^2}{2} \Delta t \right\} \right] \mathcal{F} \end{aligned}$$

The isolated potential sub-problem

$$i\partial_t\psi(x_n, t) = a(t)V(|\psi(x_n, t)|^2)\psi(x_n, t) \quad (4.6)$$

conserves the norm of ψ component-wise due to the real nature of V , $|\psi(x_n, t)|^2 = |\psi(x_n, t_0)|^2$, such that only $a(t)$ depends on time explicitly. We approximate it by the mid-point method and with the notation of Eq. (4.1) arrive at

$$\hat{U}_V(t_0, \Delta t) = \text{diag} \left[\exp \left\{ -ia(t_0)V(|\psi(x_n, t_0)|^2)\Delta t \right\} \right]. \quad (4.7)$$

t_0 is only propagated through stages \hat{U}_K and the potential is calculated at the time after those stages. Left over is the computation of the potential V . For that we condense the interaction kernels of both reduction models into a single diagonal kernel coefficient matrix $\hat{\mathbf{U}}$:

$$\text{diag}(\hat{\mathbf{U}}) = \begin{cases} 0 & n = 0 \\ -\frac{1}{k^2} & n \neq 0 \quad (1+1)\text{-SP} \\ -\frac{1}{4\pi}\mathbf{U}(1, 1, \frac{1}{2}(k_3)_n^2\epsilon^2) & n \neq 0 \quad \text{PLAM} \end{cases} \quad (4.8)$$

and apply the convolution theorem

$$V(|\psi(x_n, t)|^2) = \mathcal{F}^{-1}\hat{\mathbf{U}}\mathcal{F}|\psi(x_n, t)|^2. \quad (4.9)$$

In practice, it is not only inefficient, but also impossible to solve the above equations in k -space only, because of two non-linearity related restrictions. 1) To calculate the potential V , we need the point-wise norm $|\psi(x_n, t)|^2$ in x -space. 2) V is highly non-local in x -space and it is more efficient to apply \hat{U}_V in k -space.

This method has been developed by [Zimmermann \[2019\]](#) and partially by [Klos \[2018\]](#). Based on that code, the initial physical and numerical tests are conducted. Later in this work, the author extends the scheme with an adaptive time integration, outlined in Sec. 7.2.

4.3.2 B-Spline basis

In atomic and molecular physics the use of B-Spline basis functions [Bachau et al. \[2001\]](#) has proven to be useful. Prof. Dr. Javier Madroero from the University of Valle in Columbia and his working group use these functions as the FDM basis. The B-Spline's more localized nature makes fine tuning possible, which allows for smaller basis sizes. The field of B-Splines is extensive and we only aim to give an idea on how this method differs from the Fourier based approach. For a concise overview see [Ratnani and Sonnendrücker \[2016\]](#), [Milovanović and Udovičić \[2010\]](#).

B-Splines are polynomial functions with compact support and cardinal B-Splines are defined on an equidistant grid. A cardinal B-Spline of zero degree is the characteristic function

$$\phi_0(x) := \begin{cases} 1 & t \in [0, 1) \\ 0 & \text{otherwise.} \end{cases} \quad (4.10)$$

A cardinal B-Spline of degree $p, p \in \mathbb{N}$ is defined recursively by the convolution

$$\phi_p(x) := (\phi_{p-1} * \phi_0)(x) := \int_{\mathbb{R}} \phi_{p-1}(x-x')\phi_0(x') dx'. \quad (4.11)$$

Cardinal B-Splines are translation invariant and are easily rescaled to an equidistant grid $x_n = n\Delta x, \Delta x = \frac{L}{N}, n \in \{0, \dots, N\}$ to form a complete basis:

$$\phi_{n,\Delta x,p}(x) = \phi\left(\frac{x}{\Delta x} - n\right), \quad (4.12)$$

with support $\text{supp}(\phi_{n,\Delta x,p}) = [n, n+p+1]\Delta x$. These basis functions are not orthogonal and we denote the overlap matrix $B_{mn} := \langle B_m | B_n \rangle = \langle \phi_{m,\Delta x,p} | \phi_{n,\Delta x,p} \rangle \neq \delta_{mn}$. Therefore, the matrix representation A_{lm} of an operator \hat{A} , one has to apply in the basis $\{|B_l\rangle\}$, differs from its representation \mathbf{A}_{lm} in an orthogonal basis in the following way:

$$A_{lm} := \langle B_m | \hat{A} | B_l \rangle = \mathbf{A}_{ln} B_{mn}. \quad (4.13)$$

It is the overlap matrix, which causes off-diagonal elements in A . A consists of a $p+1$ -wide band around the diagonal and triangular parts of size p in the lower left and upper right part. Application of a matrix-vector product is much more involved compared to a diagonal matrix in the orthogonal basis.

In this chapter, we have given an overview of existing codes for the simulation of Dark Matter and why none of them meets our requirements. Our temporal and spatial discretization technique has been described. In the next Ch. 5 an inventory of that technique is performed. B-Splines, whose framework has been touched, will be tested against our method in Sec. 7.1.

5 Convergence

We start with an inventory of the numerical scheme based on the second order Fourier approach described in Sec. 4.3.1. The chosen box sizes $L \in \{100, 500, 1000\}$, which are in dimension-full units $L \approx \{2 \text{ Mpc}, 10 \text{ Mpc}, 20 \text{ Mpc}\}$, represent cosmologically relevant sizes - the typical distance between galaxies is of $\mathcal{O}(1 \text{ Mpc})$. We first look for the convergence plateau in $(N = L/\Delta x, \Delta\tau)$. Secondly, small modes of the power spectrum are compared to the linear evolution expected from classical cold dark matter. Thirdly, we check the computational performance with respect to cpu time and memory consumption.

5.1 Convergence Plateau

To find the convergence plateau in $(N, \Delta\tau)$, a fine-grained solution serves as the reference, relative to which errors are calculated. Figure 5.1 shows the error $\Delta\epsilon$, which is computed by taking the relative euclidean norm

$$\Delta\epsilon(a) = \frac{\left(\int_0^L |\Psi(a) - \Psi_{ref}(a)|^2 dx\right)^{\frac{1}{2}}}{\left(\int_0^L |\Psi_{ref}(a)|^2 dx\right)^{\frac{1}{2}}} \quad (5.1)$$

to the black-square reference. The parameter space spans three orders of magnitude in the space domain N and in the time domain $\Delta\tau$. a is the natural choice to indicate the time evolution, since it couples the non-linear potential to the Schrödinger-equation and therefore provides the best physical insight. Three box sizes are plotted row-wise.

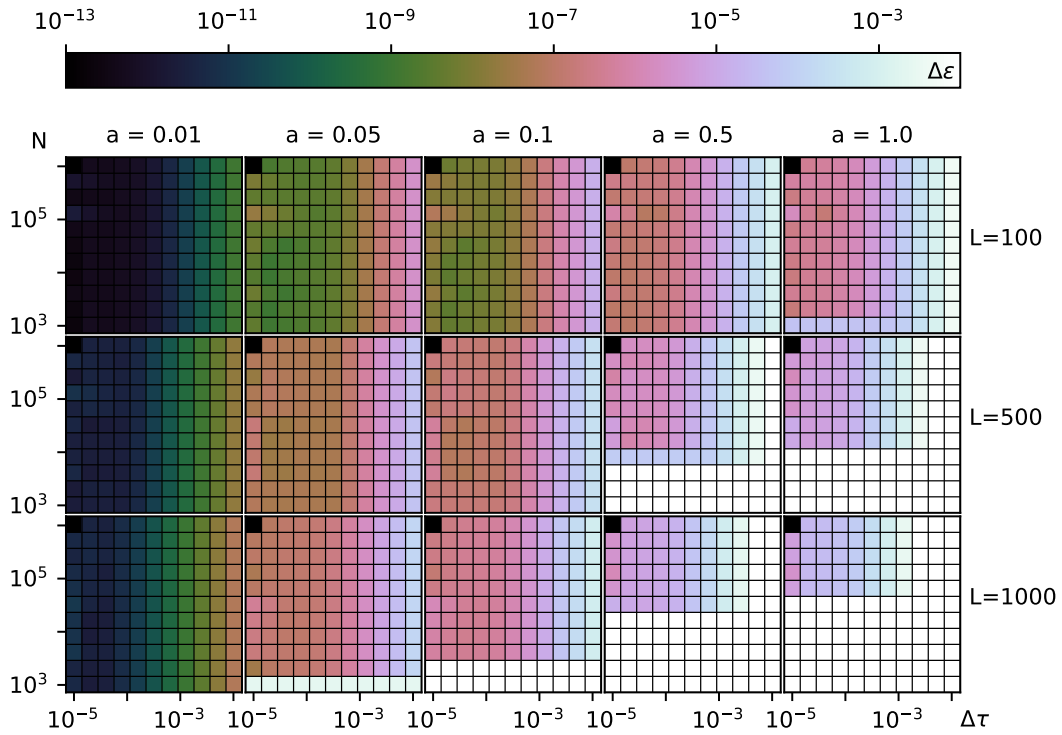


Figure 5.1: Convergence behavior with respect to different parameters in (1+1)-SP. Each cell colour-maps the errors $\Delta\epsilon$ with respect to the black-square reference. Three box sizes $L \in 100, 500, 1000$ are plotted row-wise. The time development is given column-wise in terms of the scale factor a . The N -grid is in powers of 2, due to the FFT algorithm. To make it easier to read, N and $\Delta\tau$ have ticks at powers of 10. Errors induced by constraints in Δx show in a sharp edge in N -direction, which moves toward higher N as the non-linearity increases. Issues in the time domain on the contrary create a smooth saturation with decreasing $\Delta\tau$, that does not move with time.

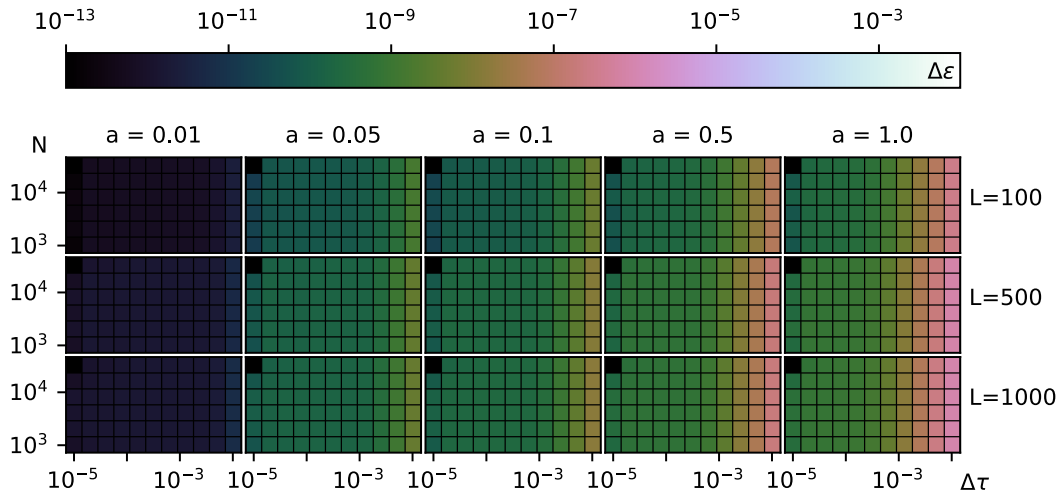


Figure 5.2: Convergence behavior with respect to different parameters under strong confinement ($\sigma = 0.01$). All remaining parameters are as in Fig. 5.1. In comparison to (1+1)-SP errors stay three order of magnitude smaller. With respect to the space constraints, the confinement model is a lot less demanding and even $N \approx 1000$ basis functions are sufficient to resolve all features. In the time domain we see the same smooth saturation toward decreasing $\Delta\tau$.

Errors arising from the space grid and time grid are clearly distinguishable. On one hand, an insufficient Fourier basis manifests in a sharp edge of $\Delta\epsilon$ in N -direction. As the problem's non-linearity grows, either when going to a larger box size or with the increasing scale factor during integration, the potential wells become deeper, and this edge moves towards greater N . The minimum requirement N_{min} is such that all modes in the power spectrum are resolved. That is the case where the natural roll-off dives into the noise floor of numerical precision. For a comparison see Fig. 7.2. On the other hand, $\Delta\epsilon$ approaches the convergence plateau in $\Delta\tau$ in a smooth manner. Even though the absolute value of the errors change, the shape of temporal convergence stays approximately constant. We deem $\Delta\tau = 8 \times 10^{-5}$ the first grid point inside the convergence plateau.

In relation to (1+1)-SP, the confinement model (Fig. 5.2) has a low demand in computational resources. Errors $\Delta\epsilon$ are three orders of magnitude smaller and results converge even for smallest basis $N \approx 1000$. The reason is its more localized interaction, as described in Sec. (2.6).

One has to consider that if the box size is changed also the underlying physics change. As the box size increases, potential wells become deeper, which is a prerequisite for any dynamics. At the same time, this adds to the computational cost, because more Fourier basis functions are needed to resolve the appearing peculiar velocities. Not only is the potential varied through the box size, but so is the cosmological initial state. How these initial states are generated can be found in Zimmermann [2019]. For small L , the state is mostly a single period sine function. The amplitude of those sine states firstly rises until $L \approx 100$. ~ 0.15 is the amplitude where the density fluctuations saturate. Beyond that, the number of periods grows to make the state highly oscillating.

5.2 Linear Theory

As a physically motivated test, we compare the power spectrum to the linear theory expected from (particle-) CDM. To get this linearized theory, one starts from the Euler-Poisson equation, sets the density to the mean density ρ_m modulo fluctuations $\delta(x, t)$, $\rho(x, t) = \rho_m(1 - \delta(x, t))$, and with some linear algebra arrives at an evolution equation of the density fluctuations $\hat{\delta}(k, t)$ in k -space:

$$\ddot{\hat{\delta}}(k, t) + 2\mathcal{H}(t)\dot{\hat{\delta}}(k, t) + \left(\frac{\hbar^2 k^4}{4m^2 a^4} - \frac{4\pi G \rho_m}{a^3} \right) \hat{\delta}(k, t) = 0 \quad (5.2)$$

This is the damped harmonic oscillator, where modes evolve independently. In the classical limit $\hbar \rightarrow 0$, the so called 'quantum pressure' vanishes and modes evolve identically. The separation ansatz $\hat{\delta}(k, a) = D(a)\hat{\delta}(k, a_{ini})$ can be applied. For a flat FLRW cosmology as in Eq. (2.35) this equation has the exact growing solution ([Dodelson \[2003\]](#))

$$D(a) = \frac{5}{6} B_x \left(\frac{5}{6}, \frac{2}{3} \right) \left(\frac{\Omega_{m,0}}{\Omega_\Lambda} \right)^{\frac{1}{3}} \left(1 + \frac{\Omega_{m,0}}{\Omega_\Lambda a^3} \right)^{\frac{1}{2}}, \quad (5.3)$$

where B_x is the incomplete Beta function. It is clear that this linearized theory is only valid on large scales, where the quantum effects are negligible. Also, the density fluctuations must not be too high in order for the linearization to hold. One expects especially the small modes k at early times to be well approximated. That is exactly what can be seen in Fig 5.3. [Garny et al. \[2020\]](#) reported the same behaviour, although in two dimensions. One difference to their discovery is that in our case modes do not necessarily stop growing after they decouple, as for example the $k = 3$ mode. Another difference is in our one-dimensional setup already the $k = 10$ mode is not related to the linear growth anymore, while in 2D larger modes still should agree and only start to decouple early.

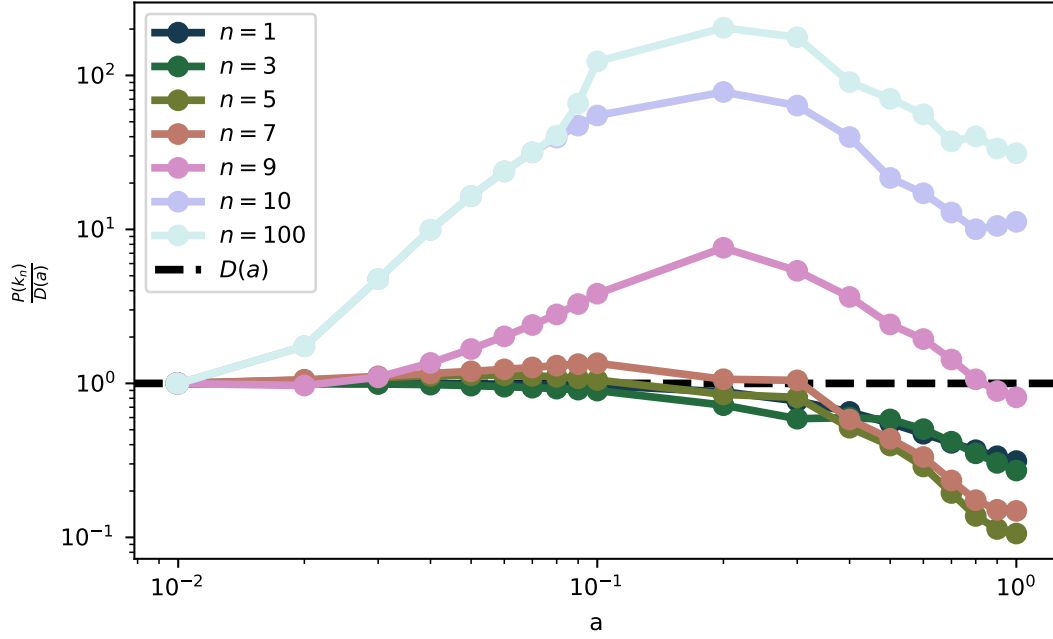


Figure 5.3: Evolution of small modes k_n of the power spectrum normalized with the linear theory, Eq. (5.3). 20 runs with varied initial states are averaged. The smallest modes show good agreement at early times until they decouple at late times.

5.3 Performance

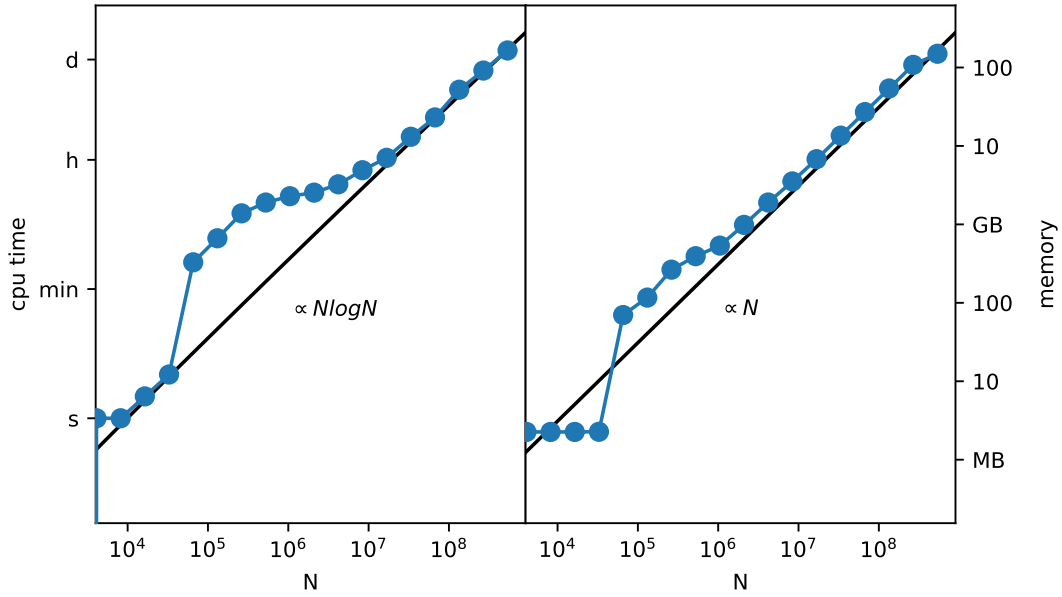


Figure 5.4: Total cpu time and memory requirements as a function of the basis size. The expected scaling functions are fitted. A time step $\Delta\tau = 10^{-2}$ was used, which allows computing large basis sizes within reasonable time. For smaller $\Delta\tau$ these plots have to be rescaled with a constant factor. Small basis simulations are more efficient, as long as important vectors fit into the processors cache (SRAM). Runs with middle sized N scale worse, because the limiting factor is memory access. At large N Fourier transforms take the most time and the scaling is as expected $\propto N \log N$

With the cosmological background in mind, the above discussed simulations represent reasonable box sizes of a few Mpc - the typical distance between galaxies - to a few tens of Mpc. All Fourier based simulations were executed on the bwUniCluster with Intel Xeon Gold 6230 processors with 1.25 MB of L1 cache, that supports basis sizes up to $\approx 2^{14}$ without additional RAM. Fourier transforms are sped up with the fast Fourier transform package FFTW and parallelized with OpenMP on 16 cores. The computational resources needed for those simulations are shown in Fig. 5.4. With a time step $\Delta\tau = 10^{-2}$, much larger than appropriate from the convergence study, even basis sizes of $\mathcal{O}(10^8)$ are feasible. The cpu time can be linearly rescaled if smaller time steps are used, while the memory consumption is unaffected by a change of $\Delta\tau$.

As for FFTs expected, the cpu time approaches a scaling $\propto \mathcal{O}(N \log N)$ and the memory (RAM) a linear scaling ($\propto N$) at large basis sizes. At medium basis sizes ($N = 10^5, 10^6$) reading and writing vectors from and to the memory plays a significant role in timing, which adds to the cpu time. Small basis sizes fit inside the cpu cache (SRAM), where no additional RAM is needed and which has a much higher access rate lowering the cpu time. Especially when moving to a higher number of dimensions both factors become limiting, as the number of grid points obviously scales with the third power in an exhaustive 3D simulation. That is why many Fourier based approaches only handle resolutions up to $N = 1024^3$, see Tab. 4.1.

A self-consistent test of the numerics around the Fourier basis and the second order

Strang splitting has been performed and the linear theory has been confirmed. We can now predict numerical challenges qualitatively and estimate them to some degree quantitatively. The next Ch. 6 uses the gained knowledge about the method's convergence and focusses on physically interesting differences between $(1 + 1)$ -SP and PLAM. As expected for FFTs, a linear scaling of memory and one $\propto N \log N$ has been found and absolute restrictions have been illuminated. The more challenging reduction model $(1 + 1)$ -SP will be used to optimize the numerical scheme, see Ch. 7, which ultimately will make higher-dimensional simulations feasible.

6 Asymptotic Dynamics

Now that the dimension reduction into the periodic line adiabatic model and the (1+1)-SP model has been completed, the numerics has been set up and the convergence has been investigated in the previous Sec. 5.1, we can now compare the two reduction models against each other, focussing on their physical intricacies. In the following, we introduce what a ground state is based on its properties and outline a method on how to ground states. Reduction to a non-cosmological space-time, where $a = 1$, eliminates the time dependency. Without that simplification, a stationary ground states could not be found. Next, to observe the interaction between ground states, we let two different mass ones collide. This chapter is concluded with an answer to the question "Do ground states act as dynamical attractors?".

6.1 Construction of ground states

The ground state is defined as the wave function φ_{GS} , that minimizes the total energy, while obeying the normalization condition, Eq. (2.33). [Choquard et al. \[2008\]](#) prove the existence of a ground state, but only under free-space condition, i.e. not in the case of the periodic interaction $G_{\Delta_1}^\pi$. Lacking the analytical tools and considering the limited scope, we just pretend that a unique, real, symmetric and positive minimizer existed.

$$\begin{aligned}\varphi_{GS} &= \operatorname{argmin}[E(\varphi)] = \operatorname{argmin}[T(\varphi) + V(\varphi)] \\ &= \operatorname{argmin}\left\{\frac{1}{2} \int_{\Omega} dx |\partial_x \varphi|^2 + \frac{a}{2} \int_{\Omega} dx (U^\pi * |\psi|^2) |\psi|^2\right\}\end{aligned}\quad (6.1)$$

The common procedure to find a ground state is by imaginary time propagation, see [Bao et al. \[2006\]](#). We set $t = -i\tau$ to arrive at an evolution operator $\hat{U} = \exp(-\tau H)$. If a ground state exists, it will be approached asymptotically when $\tau \rightarrow \infty$, because higher-energy excitations are suppressed exponentially. We refer to [Pang \[2006\]](#), [Wimberger et al. \[2005\]](#) for the numerical implementation.

An exemplary imaginary-time propagation is plotted in Fig. 6.1(A). The Gaussian state at $\tau = 0$ narrows down in x -space until it converges to a localized structure at $\tau = 1$. Panel (B) depicts the constituents kinetic energy $\langle T \rangle$ and potential energy $\langle V \rangle$ of the total energy $\langle E \rangle$, as well as the quantum virial theorem $2\langle T \rangle - \langle x\partial_x V \rangle$.

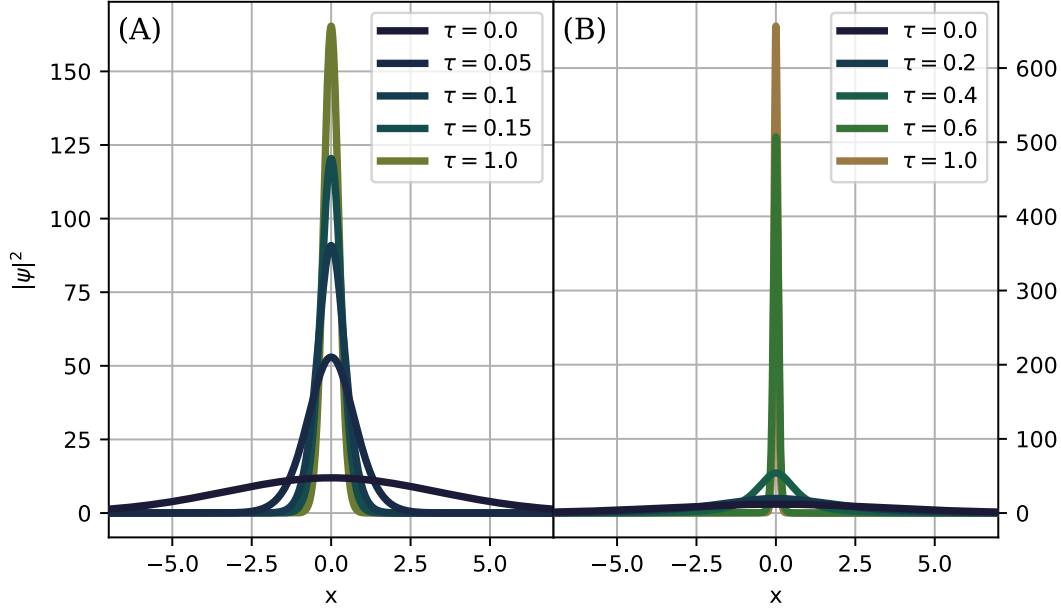


Figure 6.1: Densities at various stages of the minimization procedure with $a = 1$ and ground state mass $M = 100$. (A): The $(1 + 1)$ -SP ground state is reached quickly. (B): In PLAM ($\epsilon = 10^{-2}$) the imaginary time propagation takes longer. Note how the confinement manifests in the size of the ground state.

6.2 Inelastic Collisions

The long-term dynamics of FDM has been studied in [Zimmermann \[2019\]](#), [Zimmermann et al. \[2021\]](#). To restrict the complexity of the analysis two simplifications were introduced. Firstly, artificial, i.e. non-cosmologically motivated, initial conditions were employed. That avoids mergers of multiple overdense regions at late times and speed up the time until the first collapse. Secondly, to assure swift relaxation times the scale factor, which acts as a coupling constant to the nonlinear interaction, was fixed to $a = 1$.

It is a priori not clear what dynamical mechanisms drive $(1 + 1)$ -FDM into its asymptotic equilibrium configuration let alone whether both reduction models obey the same relaxation processes — recall the discrepancies in the interactions of $(1 + 1)$ -SP and the confinement scenario.

Given the approximative CDM interpretation of FDM, classical, non-collisional relaxation mechanisms may be a viable option, in particular a combination of phase mixing and violent relaxation, see [Lynden-Bell \[1967\]](#), [Binney \[2004\]](#). These processes induce a filamentation of the phase space dynamics alongside a redistribution of energy inside the self-gravitating structure due to its fluctuating gravitational potential.

On the other hand, $(3 + 1)$ -FDM-typical mechanisms like gravitational cooling, [Seidel and Suen \[1994\]](#), may be recovered even in one dimension, allowing collapsing matter structures to relax into an equilibrated state by radiating away excess energy in form of small scale matter waves.

Above stated calculations were performed before the author joined the research group. They will consequently not be reviewed in full detail, but rather quickly skimmed since they motivate the following discussion on the collision of ground states. (1 + 1)-Schrödinger-Poisson and the confinement model are two different pairs of shoes when it comes to their phenomenology, and we treat them accordingly.

(1 + 1) Schrödinger-Poisson The time evolution of the initially Gaussian wave function is characterized by recurring shell-crossing events in the center of the domain, which do not occur in a strictly sequential manner but are increasingly superposed and thus induce a characteristic spiralization of the phase space distribution. The structure of the early phase space distributions is qualitatively in good accordance with the evolution of one dimensional collisionless N-body systems and furthermore show the natural signature of phase mixing and (less pronounced) violent relaxation. While phase mixing manifests itself in the ever tighter spiralization of Husimi's distribution, violent relaxation induces a small yet observable increase in the occupied phase space volume. Indicated by a saturation of the energy and the entropy, an asymptotic state is achieved after only 3 – 4 shell-crossing events. Furthermore, all the dynamics take place within the domain, without crossing the boundaries, as the long interaction range of $G_{\Delta_1}^P$ does not allow ejected matter clumps to propagate till the domain boundaries.

PLAM Opposed to (1 + 1)-SP, the relaxation time is far extended. During relaxation the system exhibits a short phase of matter emission in response to the violent collapse of the initial conditions. There, multiple, stable density excitations of various masses depart from the position of first collapse, propagate outward, overcome the central gravitational potential at the domain center and proceed to travel towards the domain boundaries as unbound excitations. Closer inspection reveals the non-diffusive, form invariant nature of these excitations — solitary waves. The remaining part of the relaxation phase may then be summarized as a series of inelastic solitary wave encounters. Once the kinetic energy of a low mass stationary excitation is insufficient to escape the gravitational well of a high mass solitary wave, a merger takes place. The matter of both waves then reorganizes into a single gravitationally bound structure while expelling excess energy in form of small scale background fluctuations — the signature of gravitational cooling, [Seidel and Suen \[1994\]](#). These become visible as completely delocalized background in which all solitary waves are embedded.

We are now interested if the observed solitary waves are solitonic as well. A "soliton", as defined in [Drazin \[1989\]](#), is as a solitary wave that is invariant under interactions with other solitons, despite the nonlinear evolution. That means each wave packet conserves its energy and mass during an interaction. If that is the case and the observed solitary waves are true solitons is discussed below.

To simplify the multiple merger scenario, we investigate the collision of only two PLAM ground states. (1 + 1)-SP was assessed in the same manner, but the unstable ground states immediately turn into a single oscillatory mess when they collide. That is because in contrast to the cosmological initial states, the density contrast $\delta(x)$ is much higher. Nothing can be learned from these encounters, so let us again turn to

PLAM. Figure 6.2 shows the behavior of an asymmetric configuration of two confined ground states with initial mass $M_1 = 50$ and $M_2 = 100$ and $\epsilon = 10^{-2}$, boosted onto a collision course with:

$$\psi_0(x) = \psi_{GS,1}(x + x_0) e^{ivx} + \psi_{GS,2}(x - x_0) e^{-ivx} . \quad (6.2)$$

Figure 6.2(A) depicts the matter density in a pre-collision time window, an instance during the ground state interaction ($t \approx 17.4$) as well as a post-collision time window around $t = 32$. By the shape of the density around the interaction, it is evident that the superposition principle is not satisfied.

Post collision, both solitary waves are moving outwards with a new feature. Due to the perturbation, dispersive and contracting are no longer perfectly balanced and ψ_{GS} shows a persisting, periodic oscillation. In $(3 + 1)$ -SP the same effect has been reported [Guzmán and Ureña-López \[2004\]](#).

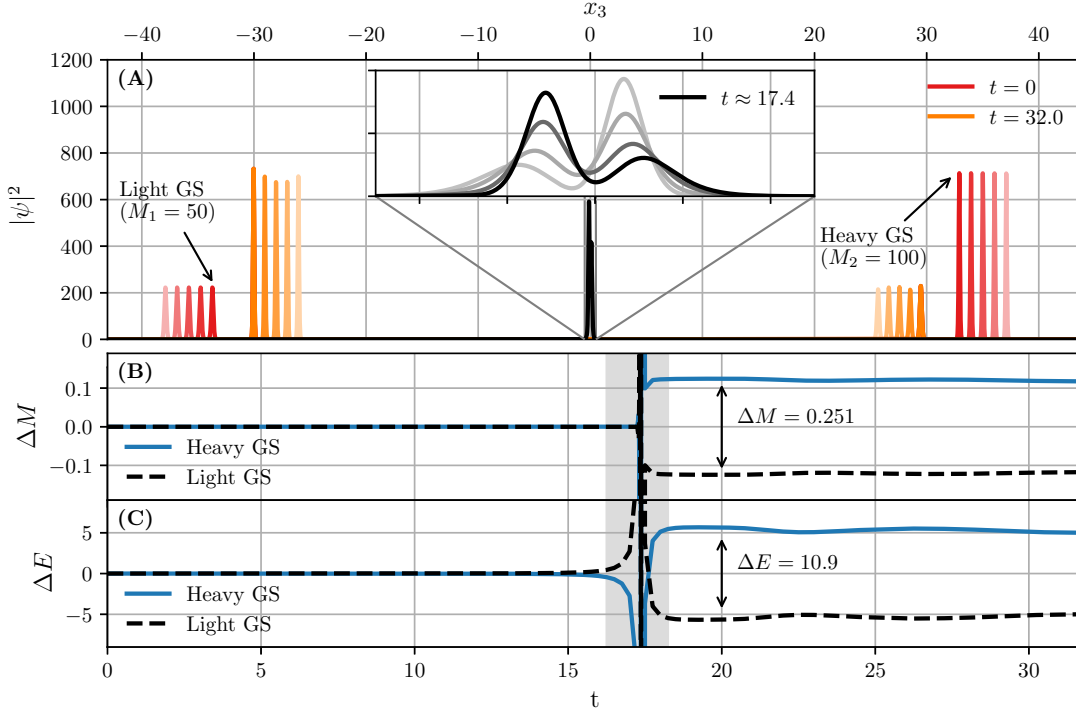


Figure 6.2: Inelastic interaction of an asymmetric high-mass, low-mass ground state configuration under strong, transversal confinement ($\epsilon = 10^{-2}$) and $a = 1$. The evolution starts from (6.2). Panel (A): Density evolution. Initially, both densities travel as solitary waves (red), pass through each other (black, inset) and continue to propagate in a quasi-solitary movement after the interaction (orange). By this we mean a state for which neither linear dispersive nor nonlinear focusing effects induce a permanent deformation of the density. Instead, one observes an oscillation around a solitary wave. Similar oscillatory behavior was found for $(3 + 1)$ -SP, [Guzmán and Ureña-López \[2004\]](#), once the ground state density is perturbed. Panel (B): Time evolution of the mass deviation of both ground states relative to their initial masses cf. Eq. (6.3). Post-interaction, it is the high-mass ground state gaining additional matter at the expense of the lighter ground state. Panel (C): Time evolution of the total energy deviation of both ground states relative to their respective initial total energies. As for the mass, the interaction induces an energy transfer from the low to high mass ground state. Notice, how the quasi-solitary behavior of the post-interaction densities is also seen in an oscillation of the energy deviation. Since the association of mass and energy contained in the positive and negative box half to a particular solitary wave is ambiguous during the interaction, we deem data in the gray shaded interval of panel (B) and (C) as not reliable. Figure taken from [Zimmermann et al. \[2021\]](#); copyright APS

To quantify the above statement that energy is exchanged during a collision of two solitary waves, we analyze the deviation in mass ΔM (Fig. 6.2(B)) and total energy ΔE (Fig. 6.2(C)) from their initial values. The states are generated separately and "glued" together afterwards, resulting in masses of exactly $M_1 = 50$ and $M_2 = 100$. In order to track the time development, the box is divided into two parts, with the cut made right where the collision takes place, x_{coll} . Doing so will let us identify the pre-collision mass of the light ground state with the total mass inside the left part of the box and

post-collision with the total mass inside the right part of the box. For the heavy ground state, left and right are swapped. That statement put into equations is

$$\Delta M_i(t) = \begin{cases} \int_{-L/2}^{x_{coll}} dx |\psi(x, t)|^2 - M_i(t = 0), & (i = 0 \text{ and } t < t_{coll}) \text{ or } (i = 1 \text{ and } t > t_{coll}) \\ \int_{x_{coll}}^{-L/2} dx |\psi(x, t)|^2 - M_i(t = 0), & (i = 0 \text{ and } t > t_{coll}) \text{ or } (i = 1 \text{ and } t < t_{coll}) \end{cases} \quad (6.3)$$

One finds, a symmetric mass and energy gap after the interaction: Both mass and energy were transferred from the low to high mass solitary wave. We note although the reported energy and mass differences are small, they are not a numerical artefact, but rather stay untouched upon variation of the space or time resolution of the integrator. Therefore, PLAM ground states are not solitons in the strict sense of the word, but interact inelastically by exchanging mass and energy during encounters, typically reshuffling them from the low-mass to the high-mass solitary wave. Furthermore we find that the peculiar velocity of solitary waves plays a role in their interaction. After each collision states have a smaller relative velocities and interact over a longer period of time, which seems to favor mass and energy transfer. If the low-mass ground state is trapped inside the gravitational well of the high-mass ground state, the interaction time is the longest and the two states merge.

6.3 Dynamical Attractors

We saw the distinct relaxation behavior of (1 + 1)-SP and the strongly confined model. Let us now focus on the transition from one to the other model and see if the solitonic solution acts as a dynamical attractor also in a weak-confinement scenario.

To make contact with the literature [Picozzi and Garnier \[2011\]](#), we need to define the ground state extent $\sigma(M)$. In (1 + 1)-SP, the Madelung picture is applicable, since $\psi \neq 0$. The hydrostatic equilibrium gives then the condition for a ground state and we infer from dimensional analysis $\sigma \propto M^{-\frac{1}{3}}$. We have no analytic solution for PLAM at hand. Instead, numerous ground states are constructed via imaginary-time propagation and their extension σ is defined by the range in which most mass is contained:

$$0.99M \equiv \int_{-\sigma}^{\sigma} dx_3 |\psi_{GS}|^2. \quad (6.4)$$

Figure 6.3 shows the asymptotic state obtained under strong, weak, and no confinement in the upper panels and gives an explanation on why ψ_{GS} acts as a dynamical attractor solely under strong confinement in the lower panels. There, the respective interaction range $R(L)$, Eq. (2.29), and ground state extent $\sigma(M)$, Eq. (6.4), are compared. The grey shaded area is not permissible, because it breaks the periodicity – the periodic box sets the limit $\sigma < L/2$.

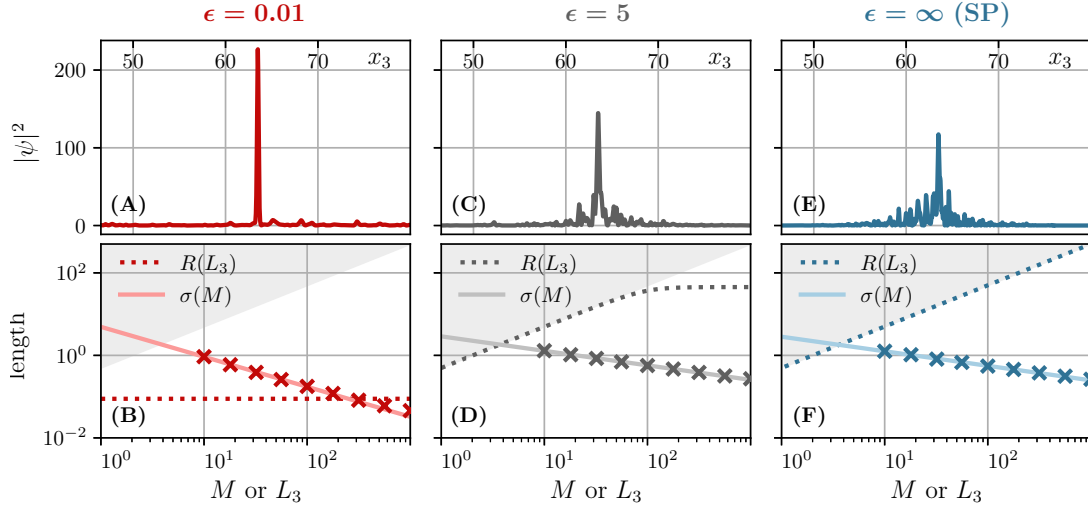


Figure 6.3: Overview of asymptotic states as a function of the confinement parameter ϵ . From left to right, we have (A)-(B) analyzing the strong confinement limit ($\epsilon = 10^{-2}$), (C)-(D) assessing the weak confinement regime ($\epsilon = 5$) and (E)-(F) evaluating the uniform reduction scenario in the limit $\epsilon \rightarrow \infty$, i.e. (1 + 1)-SP. Upper panels: Snapshot of the attained quasi-stationary states. Lower panels: Comparison of the interaction range $R(L_3)$, (2.29), and the soliton size $\sigma(M)$, Eq. (6.4). Crosses denote soliton sizes directly inferred from the gradient descent of various mass solitons. Solitons with sizes inside the gray shaded area do not exist as they violate periodic boundary conditions. For $\epsilon > 1$, we find a transition away from turbulent soliton dynamics toward a "incoherent soliton" configuration, i.e. a highly fluctuating state comprised of many density maxima beating against each other in real space. As argued in [Picozzi and Garnier \[2011\]](#), this regime is entered once the interaction range $R(L_3)$ is significantly larger than the soliton size $\sigma(M)$. Even in the best case scenario for (D) and (F), i.e. when a soliton of maximal size could form, one still finds $\sigma_{\max}/R(L_3 \approx 127) < 0.1$ — far outside the soliton regime. By contrast, the strong confinement scenario of (A) realizes $\sigma(M = 48)/R(L_3 \approx 127) > 1$ and is therefore well inside the soliton regime. Figure taken from [Zimmermann et al. \[2021\]](#); copyright APS

We find confinement parameters larger than unity to quickly approach quasi-stationary states comprising many oscillating density peaks, rather than a single, stable one. These configurations are qualitatively identical to the (1 + 1)-SP case.

[Picozzi and Garnier \[2011\]](#) found a correlation between the appearance of stable solitonic states and the ratio σ/R : If the interaction range is smaller than the ground state, $\sigma/R > 1$, stable configurations are possible and the ground state is an attractor. However, it is not given that a ground state of mass M is attained. In Fig. 6.3(A) for example, the initial state of a $L \approx 127$ box contracts into a $M = 48$ solitary wave with the remaining mass distributed in background fluctuations over the entire domain. Comparing both length scales, we have $\sigma/R > 1$, consistent with the "soliton turbulence regime". Quite often the terminology is not clear in the literature. What is actually meant by "soliton" is again, a solitary wave. On the other hand, an interaction range is bigger than the ground state, $\sigma/R < 1$ implies "incoherent soliton" and the dynamics is governed by a non-static, turbulent accumulation of mass in the center of the box.

We studied the dynamics of ground states in a static spacetime. The overused term

"soliton" does not apply, because upon closer inspection these states exchange mass and momentum during a collision. Calling them "solitary waves" is appropriate in that context. The transition between $(1 + 1)$ -SP and PLAM revealed where solitary waves can be found. The interaction range of a point-source potential has to be the same size or smaller than the size of the ground state. Extension to a dynamic space-time will mostly slow the dynamics down, i.e. lower the exchange of mass during a collision, but we do not expect new qualitative features. The next step towards an understanding of the full-fledged model is therefore to move to higher dimensions, e.g. $(2 + 1)$ -SP or $(3 + 1)$ -SP.

7 Code optimization

With the aim of high computational performance in mind, two aspects qualify for further improvement of the integrator. The space grid and the time grid. Both are analyzed below.

7.1 Improve spatial discretization with B-Splines

In this section we consider refining the space discretization. A priori it is not clear which function basis fits the problem, but in atomic physics B-Splines have been used successfully to solve the Schrödinger equation (see [Bachau et al. \[2001\]](#) for an introduction).

The B-Spline method presented here has been implemented independently by the group around Prof. Dr. Javier Madroñero from the faculty of natural sciences in Valle, Columbia. Therefore we will not give any technical details beyond what has been stated in Sec. 4.3.2, but rather compare their endresults with ours. The following serves as a sanity check and validation for both, the Fourier code as well as the B-Spline code. We test the B-Splines against the Fourier basis, firstly by a direct comparison of their densities $\rho = |\psi|^2$ in x -space and in k -space and secondly by their conservation of mass and momentum.

7.1.1 Direct Comparison in x -space

As a first measure we compare the wave function with the Fourier base, ψ_{Fb} , to the wave function with the B-Spline base, ψ_{BS} , via

$$\Delta(x, t) = |\psi_{Fb}(x, t) - \psi_{BS}(x, t)|^2. \quad (7.1)$$

In Fig. 7.1 both wave functions are shown, as well as their difference at various stages of the integration, given in terms of the scale factor a . In the first one at simulation start, $z = 100$ ($a \approx 0.01$), numerical errors of $\mathcal{O}(10^{-23})$ appear, which are within numerical precision. At $a = 0.1$, the overdense region begins to collapse. And as expected in the areas of depletion and accumulation of mass, the difference between the codes begin to show, whereas average-density regions $\rho = |\Psi|^2 = 1$ continue to coincide. The solutions are close and the difference grows to $\mathcal{O}(10^{-5})$ at the end of the simulation. Since the two independently developed methods give comparable results, we deem both implemented properly. In the second one, Δ grows to $\mathcal{O}(10\%)$, but the solutions are still correlated and peaks in Δ occur where $|\psi|^2$ is large. That is no longer the case in the largest box. The zoom-in is at $a = 0.6$, where Δ is already above 100%. Past that the methods differ strongly and Δ is no longer correlated to $|\psi|^2$. The reason why the methods drift apart is discussed in the following.

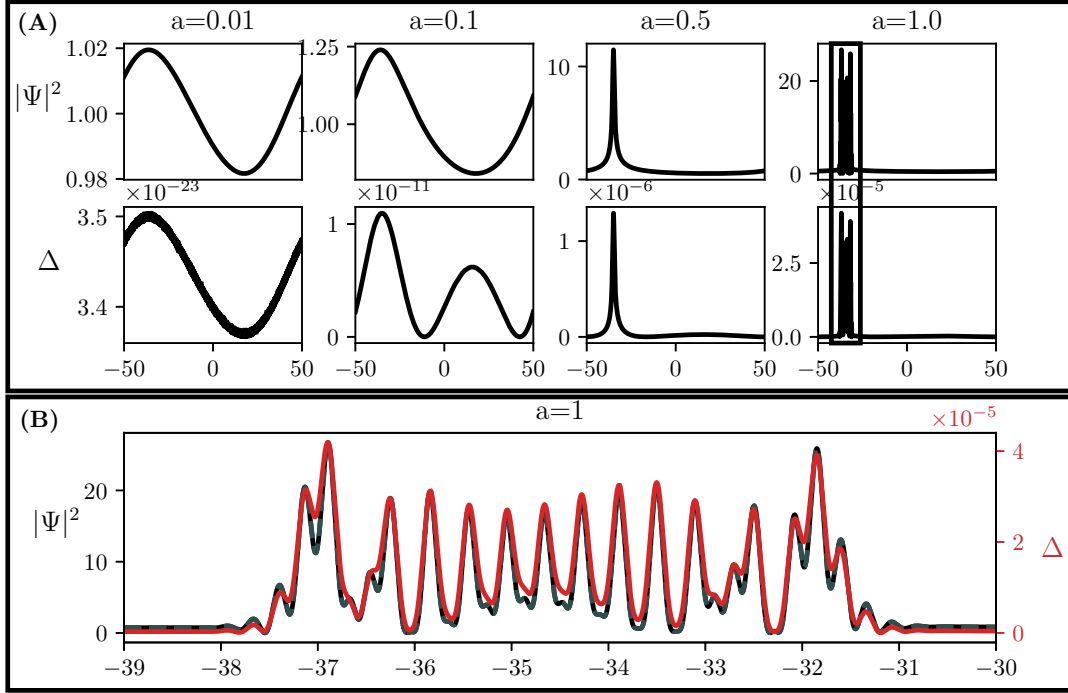


Figure 7.1: (A): Wave function in a small box ($L=100$) of the B-spline as well as the Fourier method and their difference Δ at various stages of the integration given in terms of the scale factor a . Differences between the solutions are limited by numerical precision in the beginning of the simulation and grow to $\mathcal{O}(10^{-5})$ at the simulation end. (B): Zoom into the black box at $a = 1$. Differences in the two methods are approximately proportional to the density itself.

7.1.2 Power Spectra

All power spectra, see for example Fig. 7.2, are symmetric, because $|\Psi|^2$ is real, so that there are $k_{max} = \frac{N}{2}$ modes in Fourier space. The Fourier basis approach (thick blue lines) underlies the B-spline method (thin grey lines). a serves again as the time parameter. The number of B-spline basis functions $N_{Spline} \in \{40000, 90000, 125000\}$ was set in such a way, that a Fourier basis of that size can resolve the entire spectrum.

In the lower part of the spectrum $k < \frac{N_{Spline}}{2}$, the power spectra of both methods follow each other closely. But there is more spectral content available when the B-Splines are sampled above. We detect peaks in the spectra at $k = nN_{Spline}$, $n \in \mathbb{N}$, which exist early on and grow in time not only in amplitude, but also in extent. They originate in an inherent lack of resolution of the B-Spline basis at those scales. The natural roll-off and peaks are distant in Fig. A.3 and peaks remain confined. In Fig. A.4 the natural roll-off and B-Spline peaks are closer, which favors the growth of the latter. The two even overlap in Fig. 7.2. Rather unfortunate for the precision of the simulation, the power of the resulting peaks has a comparable amplitude to the small modes and they extend over a large range in k -space. At this point it is only clear that resolution issues in the B-Spline method are more severe in larger boxes, whether they are caused by the higher amount of dynamics or because the natural roll-off is closer, has to be studied further. It is obvious on the contrary that the size of a Fourier basis can be limited to the roll-off, which makes it more suitable to solve the Schrödinger-Poisson equation

than the B-spline basis.

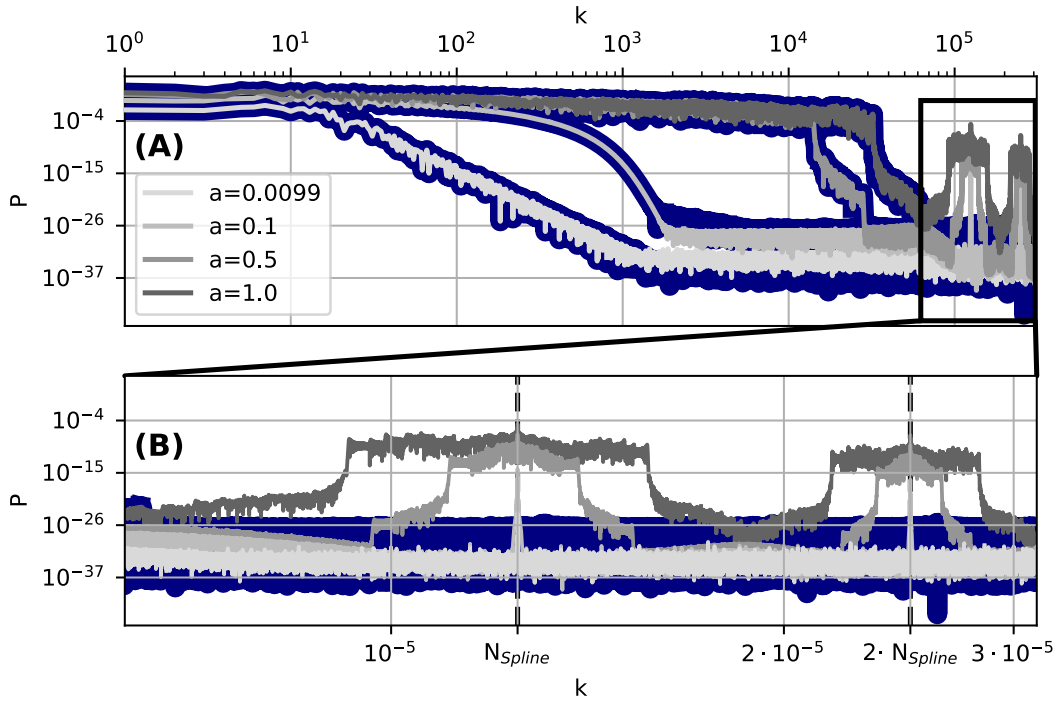


Figure 7.2: (A): Evolution of the power spectra in the large box ($L = 1000$) in terms of the scale factor a . The Fourier basis method (blue) underlies the B-splines in grey color. Modes $k < N_{Spline}/2$ coincide in their spectra. (B): Zoom-in of the 'oversampled' B-Splines. Peaks show up at multiples of the grid size at $k = nN_{Spline}$, $n \in \mathbb{N}$ (black dashed lines). They exist early on and expand during integration.

The expected advantage of B-splines was that it demanded a smaller basis size to resolve the structures in ψ - an assumption that is now proven wrong. The Fourier basis does indeed work better in the context of the Schrödinger-Poisson equation. If we still were to enhance the spatial discretization, there are several possibilities: The B-Splines' degree can be raised to resolve highly oscillatory wave functions at the cost of a greater function support and increased complexity due to wider bands in the operator matrices. Moving from the cardinal B-Splines to a non-uniform grid is conceivable, but this only makes sense if the grid points adjust according to the wave function's development - a highly complex endeavor.

That brings us to the most common technique, the adaptive mesh refinement as in Schive et al. [2018b], Veltmaat et al. [2018], Bryan et al. [2014b], where certain grid elements are subdivided, sometimes on multiple levels and eventually integrated with a different time step. Also the boundary conditions for this sub-grid are now of fixed Dirichlet type and the Fourier method from Sec. 4.3.1 can not be applied. A finite differencing scheme is needed. The Problem is that one has to track the development of ψ with different integrators and possibly on varied time steps. Storing these informations increases the complexity.

For the beginning it is reasonable to look into non-uniform discrete Fourier transforms that work non-equispaced grids, e.g. the NFFT package, but attention has to be paid.

For nonuniform FFTs the adjoint NFFT is not necessary the same as the inverse as with uniform FFTs. Basis sizes $N = 10^9$ are the memory limit of the "thin" nodes on the bwUniCluster. If one of those revisions is necessary, depends on how our code scales in higher dimensions. On the physics side the interaction potential becomes more localized in 2D and 3D and need in theory smaller basis sizes, which would play into our hands.

Thanks to our colleagues from Columbia, we were able to sanity-check our numerical implementation. Because the current B-Spline code has issues on some scales, it is less efficient. If these problems were fixed, results could look promising, especially when conserved quantities are of interest, see Sec. 7.3. In the following, we will stick to our Fourier method and deal with the second improvement, the time stepping.

7.2 Enhance time stepping

The second improvement of our numerical procedure is in the temporal discretization. We compare the 4th order integrator of the newly implemented embedded splitting scheme "Emb 4/3 BM PRK/A" from [Auzinger et al. \[2016a\]](#) to the standard Strang splitting, Eq. (4.1), used for all results above. Furthermore, we estimate the error at each time step using the combined 4th / 3rd order method, which we use to adaptively set the time step size $\Delta\tau$.

7.2.1 4th-order integrator

A generalized splitting scheme of order p has the following form:

$$\mathcal{U}_{K+V} = b_s \mathcal{U}_K \circ a_{s-1} \mathcal{U}_V \circ \dots \circ a_1 \mathcal{U}_V \circ b_1 \mathcal{U}_K + \mathcal{O}(\Delta t^{p+1}), \quad (7.2)$$

where a_i and b_i are the splitting coefficients. In comparison, in Eq. (4.1) they are $a_1 = 1, b_1 = b_2 = \frac{1}{2}$. s is the number of stages, which only coincides with the accuracy p at certain low-order schemes. A plethora of higher-order integrators has been deduced, which is a non-trivial task. [Auzinger et al. \[2016a\]](#) gives some insight on the construction of these schemes and we refer to [Auzinger \[2021\]](#) for a collection of splitting coefficients. We choose a fourth-order method, since it offers a significant upgrade in performance while also being compatible with an adaptive time-step selection explained in the following. The splitting scheme "Emb 4/3 BM PRK/A" from [Auzinger et al. \[2016a\]](#) is an embedded scheme, meaning it has two co-working integrators. One is third-order accurate (4 stages) and acts as the controller, the other is fourth-order accurate (7 stages) acting as the worker. They share the three first splitting coefficients, which reduces the effective number of stages needed per time step.

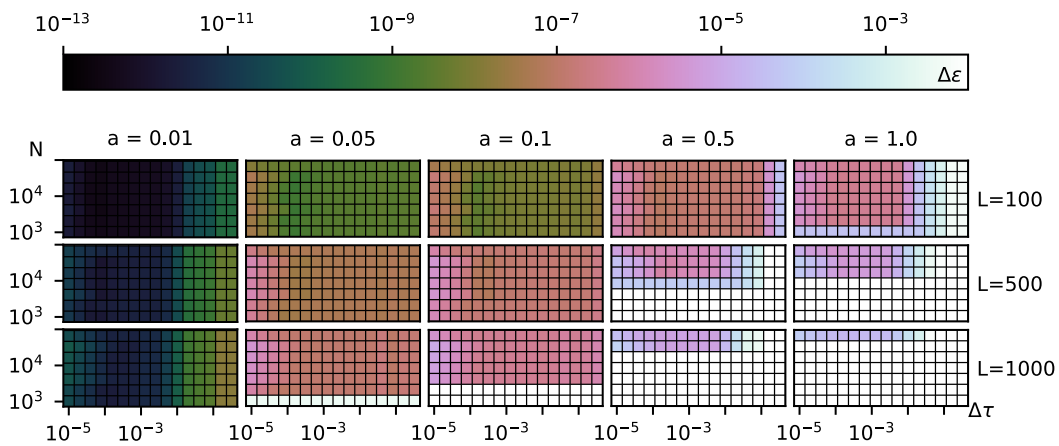


Figure 7.3: Convergence of the fourth order integrator relative to the same reference as in Fig. 5.1. The space domain behaves exactly as before. On contrast, the convergence is much faster with regards to the time step, such that the plateau is reached at $\Delta\tau \approx 5 \times 10^{-3}$.

To get a feeling for higher order splitting scheme, let us first consider the worker on its own with a constant time step. Figure 7.3 reveals its convergence behaviour relative

to the black-square references of Fig. 5.1. As a confirmation of the previous interpretation of the convergence plateau, we observe the exact same behaviour in the spatial domain: There is a sharp edge in $\Delta\epsilon$ in N -direction, because of the minimum requirement to resolve all modes below the natural cut-off of the power spectrum. In the time domain, the situation is different. Convergence is much faster in $\Delta\tau$, which is expected and the only reason for this more involved scheme.

We can make an estimation of the speed up factor by comparison of the minimum time-step requirements of solutions with the same accuracy. For the Strang splitting that is the $\Delta\tau = 8 \times 10^{-5}$ one and for the fourth order one the plateau begins at $\Delta\tau \approx 5 \times 10^{-3}$. It is important to include the number of FFTs per time step into the estimation, which is 12 and 2, respectively – FSAL properties included. All in all that results in a speed up factor of ~ 25 .

7.2.2 Adaptive Step Size

An adaptive time-step selection is then implemented by comparison of the 4th- and 3rd-order integrator. The advantage of such an inherent error estimation is that the Courant-Friedrichs-Levi (CFL) criterion based on finite differencing schemes, as used in [Schive et al. \[2018b\]](#), [Mina et al. \[2020\]](#), [Li et al. \[2019\]](#), is not needed. The selection of the next $\Delta\tau_{new}$ based on the current one $\Delta\tau$ is then

$$\Delta\tau_{new} = \min \left\{ \alpha_{\max}, \max \left[\alpha_{\min}, \left(\frac{\alpha \cdot tol}{\Delta\epsilon} \right)^{\frac{1}{order+1}} \right] \right\} \Delta\tau. \quad (7.3)$$

The same $\Delta\epsilon$ as in Eq. (5.1), but applied to the wavefunction calculated by the 3rd and 4th order method, acts as a local (in time) error measure and the parameters are $\alpha_{\max} = 4$, $\alpha_{\min} = 0.25$ and $\alpha = 0.9$. [Auzinger et al. \[2016b\]](#) stated that their exact value is not important, but it is imperative to have them included in the metric to avoid oscillatory behavior, which we can confirm. The time step is mostly self organizing well within the limits of these parameters. Only occasionally when ψ becomes quasi-stationary, $\Delta\tau$ tends to jump up and is then slowed down by α_{\max} , or when two density peaks merge, jumps of $\Delta\tau$ downwards are limited by α_{\min} . tol then sets the desired accuracy and order accounts for the order of the chosen splitting scheme. The initial time step can be chosen relatively large, but time step self-organization takes a few steps, during which errors can accumulate. $\Delta\tau_{ini} = 10^{-3}$ is sufficient for most purposes.

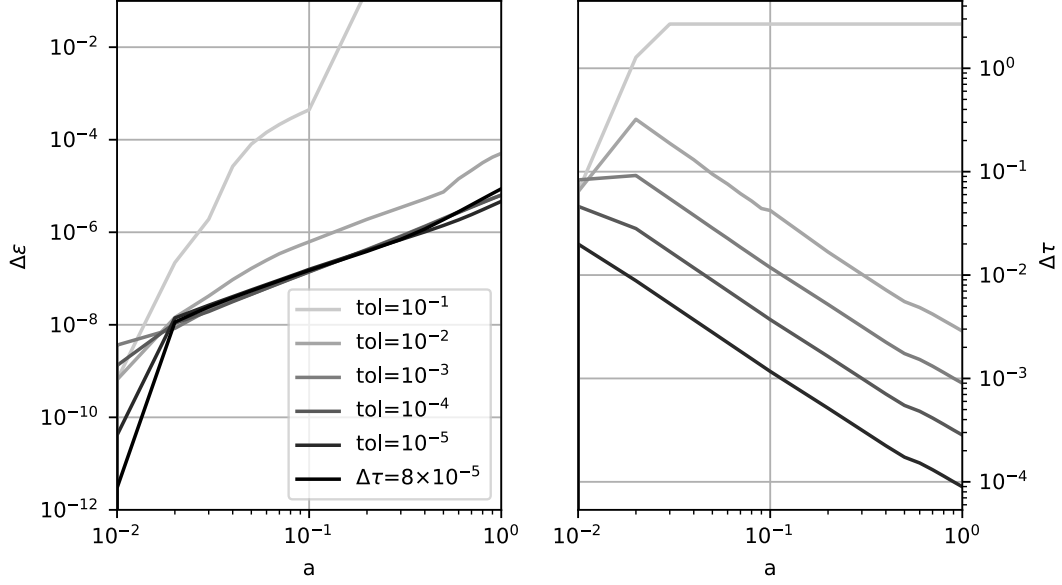


Figure 7.4: Left: Deviation from the reference solution as a function of the scale factor (time) in the $L = 500$ box. Five adaptive, 4th order solutions with different tol parameters are shown and one converged second order solution with a constant time step $\Delta\tau$. Right: Evolution of the time step $\Delta\tau$ during integration. Here, time step selection works well for $tol \leq 10^{-2}$.

We investigate the behavior of the adaptive integrator in the following manner: A box size $L = 500$ is chosen. For $L \in \{100, 1000\}$ cf. Fig. A.6, A.7. To guarantee convergence in the space domain, we set $N = 2^{20} \approx 10^6$. The initial time step is $\Delta\tau_{ini} = 10^{-3}$. A sweep of tolerance parameters $tol \in \{10^{-1}, 10^{-2}, 10^{-3}, 10^{-4}, 10^{-5}\}$ controls the time step size. With that, the relative euclidean norm $\Delta\epsilon$ of the the reference solution (Strang splitting, $\Delta\tau = const. = 10^{-5}$, $N = 2^{20}$) and the adaptive solution is calculated and plotted over the scale factor. A second order solution with $\Delta\tau = 8 \times 10^{-5}$ serves as a guide. Figure 7.4 shows how this guiding solution is approached by the adaptive ones, when tol is sufficiently small. The maximal accuracy of any solution is limited by the fidelity of the reference itself, which is estimated by $\Delta\epsilon$ of a nearby solution within the convergence plateau (Fig. 5.1), e.g. our guiding solution. Consequently, the reference is $\mathcal{O}(10^{-5})$ accurate at the simulation end.

In the right half of Fig. 7.4 one can see how the time step evolves with time. All lines depart from $\Delta\tau(a_{ini}) = 10^{-3}$. If the tolerance allows for it, The time step grows until $a \approx 0.02$ for large tol . If $\Delta\tau \geq 1$, calculation of the step size becomes unstable and $\Delta\epsilon$ fails to serve as a local error estimate. For which tol this is the case depends on the box size L . If $\Delta\tau \leq 1$, the time step is reduced monotonically - with minor fluctuations on top - as the non-linearity increases (with increasing scale factor).

Total cpu time and speed up factor are shown in Fig. 7.5. We derive the tolerance from the previous figures, such that the time step is still self-controlling (from $L = 100$ to $L = 1000$: $tol \in \{10^{-3}, 10^{-2}, 10^{-1}\}$). The cpu times of the three boxes align and the speed up factors are of $\mathcal{O}(50)$. Albeit not the most precise solutions, they only differ by $\Delta\epsilon = \{10^{-6}, 10^{-5}, 10^{-5}\}$ from the reference at the simulation end. For a similar plot to Fig. 7.5, but with $tol = 10^{-3}$ for all boxes, see Fig. A.5.

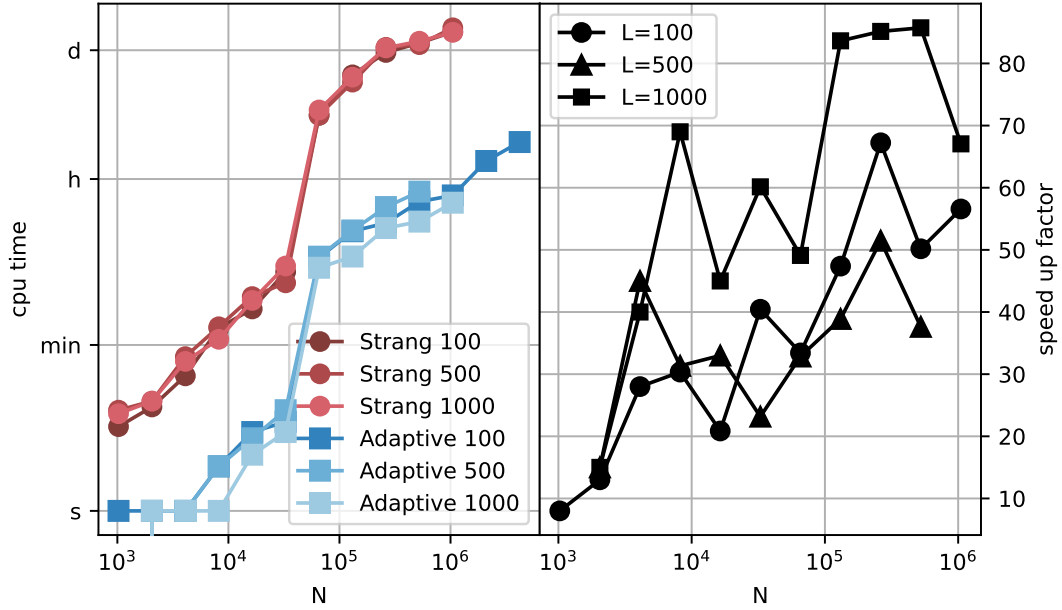


Figure 7.5: Cpu usage and speed up factor of the three boxes sizes $L \in \{100, 500, 1000\}$. Tolerance parameters are chosen as $tol \in \{10^{-3}, 10^{-2}, 10^{-1}\}$ - within the stability region, where $\Delta\tau \leq 1$. Remarkable speed up factors around 50 are possible.

Now we know how to handle the time-step selection and which tolerance parameter to choose for a given desired accuracy. This numerical method we have at hand is 10 ~ 50 times faster than the Strang splitting (Eq. (4.1)), which allows for large scale simulations and even large scans of parameter spaces in reasonable time. Higher-dimensional simulations will profit greatly of this improvement. Since the new integrator is not symplectic, meaning its phase space volume is not necessarily conserved, conservation of mass and momentum are assessed in the upcoming section.

7.3 Conserved Quantities

The new integrator based on a fourth order operator splitting is in contrast to the standard Strang splitting not symplectic and the phase space volume is not conserved. Of special interest is consequently, how the two constituents behave: The spatial constraint Eq. (2.33) is equivalent to the conservation of mass, while the second bound is the conservation of momentum.

7.3.1 Conservation of Mass

A physical way to assess the accuracy of the integrator is by checking how well mass is conserved.

$$|\Delta M(a)| = \left| \int_{\Omega} |\psi(x, a)|^2 - |\psi(x, a_{\text{start}})|^2 dx \right| \quad (7.4)$$

We can expect mass conservation, since the time evolution operator is unitary by design. Figure 7.6 shows how the mass evolves with time, beginning at $|\Delta M| = 0$. Besides the Fourier method and the B-Spline method the new adaptive method is given. The Fourier method shows a strong increase of $|\Delta M|$ right at the simulation begin, but saturates soon, such that overall the mass is well conserved – $|\Delta M| < 10^{-6}$ in all cases. Small boxes are handled exceptionally well by the B-spline method, where the spatial resolution is high enough. Large box sizes need a much higher resolution, which was not foreseeable. Consequently B-Splines can not keep up and $|\Delta M|$ rises to $\mathcal{O}(10^{-3})$. The new adaptive method combines the advantage of both. $|\Delta M|$ starts low, comparable to B-Splines, and does not grow too strongly, comparable to the Fourier method. At simulation end we have $|\Delta M| = \mathcal{O}(10^{-9})$.

Differences between the Fourier and adaptive method originate solely from the time discretization. We can conclude that mass conservation is fulfilled better if the time-step size is larger and less Fourier transform are executed. Fig. 7.8 substantiates this claim. The slope of #FFTs is very reminiscent of the one observed in $|\Delta M(a)|$ for the adaptive method. In relation to the standard splitting, the new adaptive scheme needs $\mathcal{O}(10^3)$ times less Fourier transforms. That number is already corrected for the number of FFTs for each time step – 2 and 17, respectively.

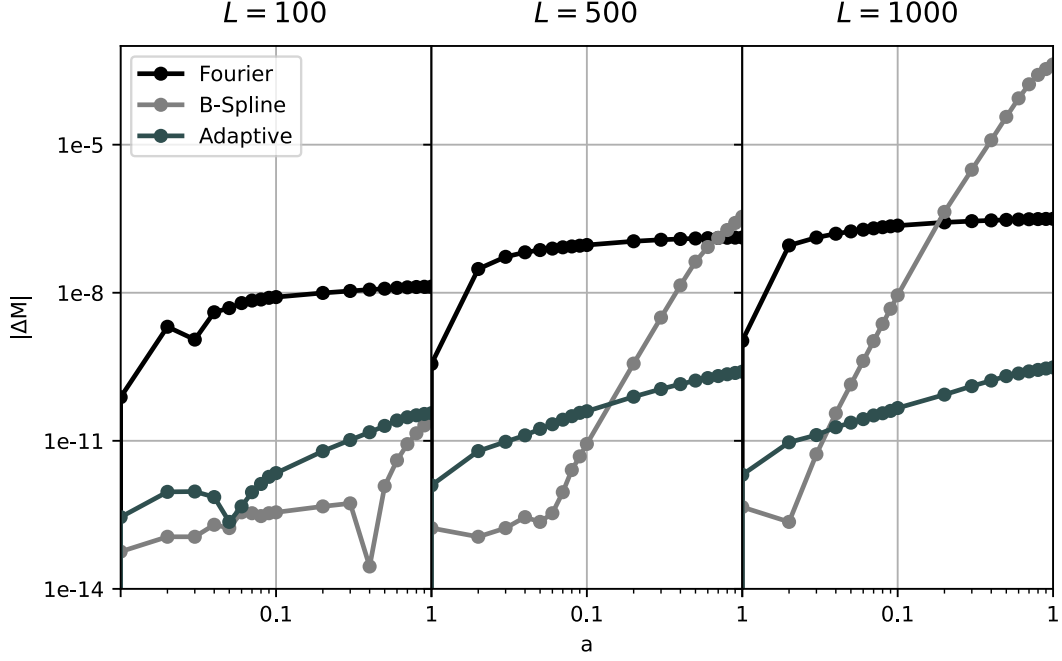


Figure 7.6: Conservation of mass of Fourier, B-Spline and the new adaptive method for three box sizes. The Fourier method conserves the total mass below the 10^{-6} range, whereas the B-spline method is in advantage for smaller L , but struggles with the larger boxes, where $|\Delta M|$ grows to $\mathcal{O}(10^{-3})$. The adaptive method is the most advanced solution. It starts at $|\Delta M| = \mathcal{O}(10^{-12})$ and stays bounded by $|\Delta M| = \mathcal{O}(10^{-9})$.

7.3.2 Conservation of Momentum

Linear momentum, despite being a derived quantity, is conserved in an expanding space, see [Zimmermann \[2019\]](#).

$$P = -\text{Im} \left(\int_{\Omega} \partial_x (\psi(x, a)^*) \psi(x, a) dx \right)$$

$$|\Delta P(a)| = |P(a) - P(a_{\text{start}})| \quad (7.5)$$

How the spatial derivative ∂_x is implemented, influences the resulting momentum to a high degree (Fig. A.8). For Fig. 7.7 we calculated the momentum, or more precisely the partial derivative, in k -space directly, since it is the most accurate. To some degree the behaviour is as in Fig. 7.6 before. $|\Delta P|$ of the Fourier basis method grows gradually until $\mathcal{O}(10^{-7})$. The B-Spline method initially stays below that, but in the more complex territory, where more basis functions are necessary, we have $|\Delta P| = \mathcal{O}(1)$. This effect is more pronounced than for the conservation of mass, because the conservation of momentum is more involved. Besides ψ also its derivative $\partial_x \psi$ has to be represented accurately.

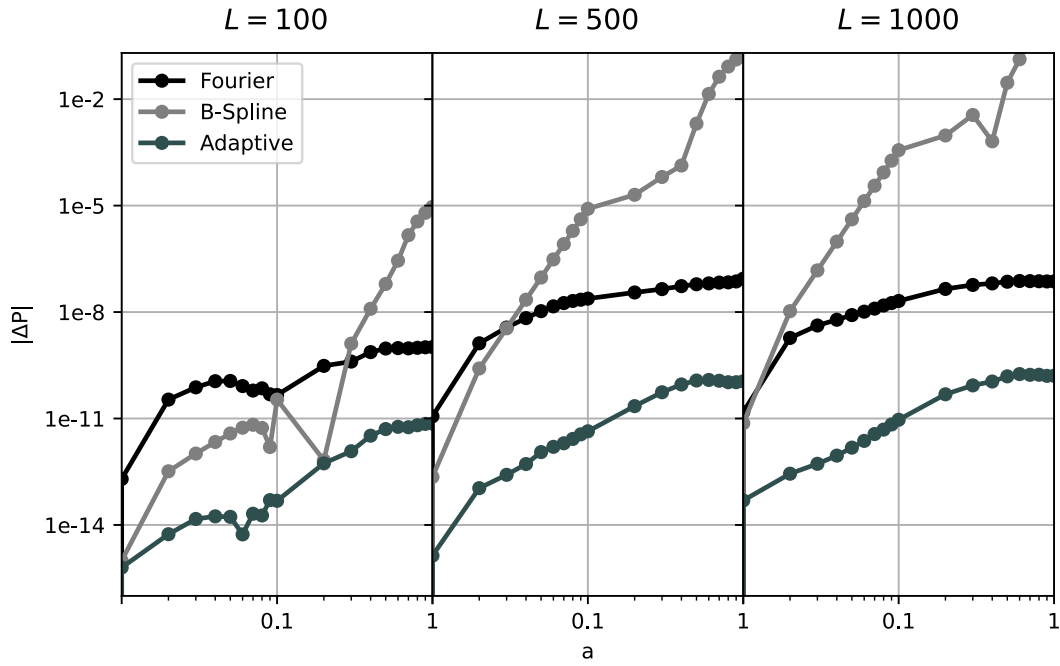


Figure 7.7: Momentum conservation of the Fourier, B-Spline and the new adaptive method for the three box sizes. The momentum is calculated in k-space directly by application of the momentum operator. The situation is qualitatively similar to Fig. 7.6, but problems in the B-Spline method arise earlier than in the conservation of mass, because the momentum is a derived quantity.

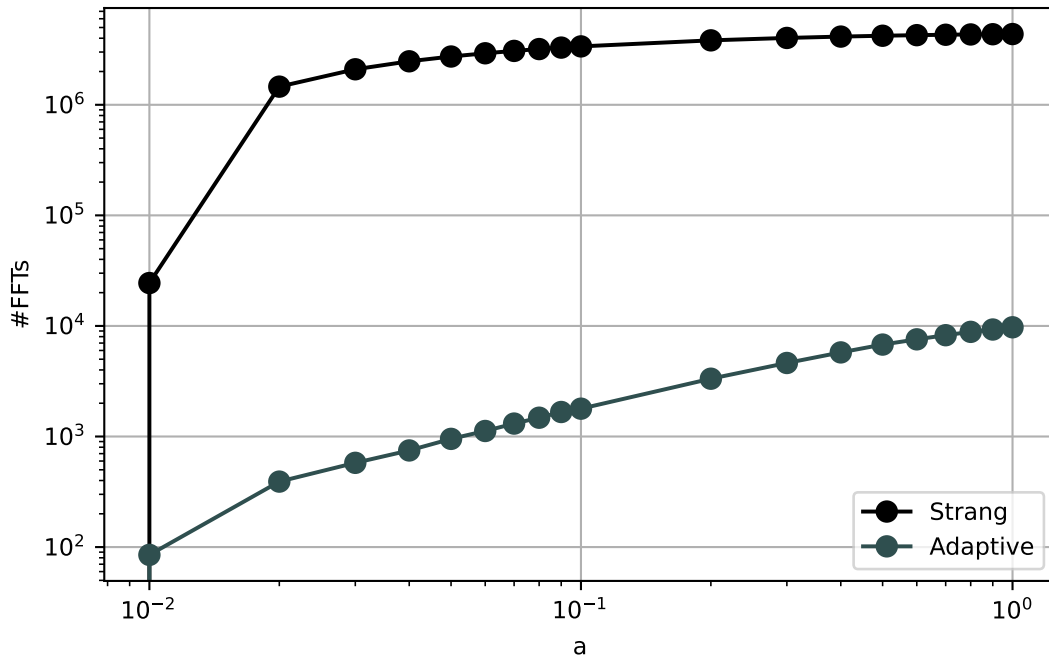


Figure 7.8: Number of FFTs for the standard Strang splitting and the adaptive method, which has $\mathcal{O}(10^3)$ less FFTs. Also, #FFTs grows significantly, even at late times, in the case of time adaptivity.

Mass conservation surprisingly is best guaranteed in the B-Spline method, at least

in small boxes where its problems show only mildly. Close to that comes the adaptive method, which is also somewhat unexpected, have we just noted the lack of its symplecticness. Mass is about three orders of magnitude better conserved than in the Strang method. The reason was found in the substantially reduced number of Fourier transforms.

Of all integrators, the time-adaptive, 4th-order scheme performs the best. It is 10 – 50 times faster than the standard Strang splitting, or alternatively more accurate when using the same resources. Mass and momentum are by a factor $\sim 10^3$ better conserved. In comparison to the B-Spline method, the power spectrum is clean without any peaks above the natural roll-off. How many basis functions are required for a certain problem can be roughly estimated and the tolerance parameter takes care of the time step selection.

8 Conclusion and Outlook

The assessment of the Schrödinger-Poisson equation is by no means exhausted and there is still terrain left to be explored. We are now at a point, where the one-dimensional models are understood well enough to extend the domain into two dimensions. In the following, a recap of this work is given, followed by first considerations towards $(2 + 1)$ -SP.

8.1 Summary

In this thesis, two reduction models of the three dimensional Schrödinger-Poisson equation were studied. Both resemble Fuzzy Dark Matter in one dimension, but differ in their phenomenology. PLAM, where two dimensions are confined by a harmonic potential, was further investigated. As a follow-up to the relaxation mechanisms and long-term dynamics of gaussian initial states in [Zimmermann et al. \[2019\]](#), we demonstrated how two stable, solitary solutions interact with each other and thereby exchange mass and momentum. Also, in accordance to [Picozzi and Garnier \[2011\]](#), the criterium for the stability of a solitary solution was confirmed. If the relation of ground state size and interaction range is larger than one, stable solitary waves are found, but if the relation is smaller than one, which preferably happens with weak transversal confinement, the system transitions to 'incoherent soliton dynamics'. ψ is no longer a single peak structure, but rather many oscillating peaks, that beat against each other in the center. Although the PLAM model has features also found in $(3 + 1)$ -SP, e.g. the stable solitary states, and helps understanding the physical phenomena, it remains a toy model, that can not replace $(3 + 1)$ -SP in quantitative aspects.

In order to clear the way for higher-dimensional simulations the numerical method was improved with respect to two points. The first is the spatial discretization. In collaboration with a Columbian working group, we tested a B-Spline basis method against our Fourier basis method. At high resolution and weak nonlinearities, the B-Spline method conserves mass and linear momentum to a higher degree. However, when moving into the strongly nonlinear regime, the Fourier method takes the lead. Besides a better conservation of the physical quantities, also the computational efficiency is higher and less basis functions are needed. The issue of arising peaks in the matter power spectrum of the B-Spline method is still up to debate. If that can be fixed, a reassessment would be necessary. The second criterium is the time integration. A 4th-order embedded scheme from [Auzinger et al. \[2016a\]](#) was implemented, which constitutes an adaptive time-step selection. Computation times are greatly reduced by a factor of up to $\mathcal{O}(50)$ relative to the standard Strang splitting. A positive side effect of the larger time steps is that mass and linear momentum are better conserved, because ψ undergoes $\mathcal{O}(10^3)$ less Fourier transforms.

8.2 Future Extension

What to do next? The logical consequence and what motivated us to improve the numerical method is the higher-dimensional model, $(2 + 1)$ -SP. That goal is now within reach, but it is yet unclear how the dynamics change from one to two dimensions, especially considering the computational boundaries. We stated that the memory constrains simulations to $\sim 10^9$ basis functions or $\sim 10^4$ in each dimension. Consequently, if memory consumption becomes a problem, there is no way around the improvement of the basis representation, either by modifying the B-Splines, or an adaptive mesh refinement. What might play into our hands is that in two dimensions the interaction potential is more confined. Due to that, seeing $(3 + 1)$ -SP as an upscaled version of $(1 + 1)$ -SP can overestimate the numerical demand.

How does our numerical scheme change in higher dimensions? Let us consider the two-dimensional case. Moving to 2D means an extended spatial domain with side lengths L_1 and L_2 :

$$\mathbf{x} \in \Omega = [0, L_1) \times [0, L_2) \quad (8.1)$$

in general. Wave function ψ , potential V and interaction kernel \hat{U} are currently all vectors of size N , or behave as such. In 2D, vectors become matrices of size $N_1 \times N_2$, which might be represented by lengthened vectors:

$$\psi(\mathbf{x}) = \psi(x_{\mathbf{n}}) = [\psi(x_{0,0}), \psi(x_{0,1}), \dots, \psi(x_{0,N_1-1}), \psi(x_{1,0}), \dots, \psi(x_{N_1,N_2})]^T. \quad (8.2)$$

Falling back to such a vector-like notation suggests, that all operators can be applied as before. That is not the case. Even the evolution operator of the linear kinetic sub-Hamiltonian, \hat{U}_K , contains now the matrix exponential of the full matrix $k_{\mathbf{n}}$:

$$\hat{U}_K = \mathcal{F}^{-1} \exp\left\{-\frac{i}{2} k_{\mathbf{n}}^2 \Delta t\right\} \mathcal{F}. \quad (8.3)$$

It is a constant coefficient matrix, which can be computed once. Generally, the exponential of a matrix A is given by the infinite series:

$$\exp(A) = \sum_{m=0}^{\infty} \frac{A^m}{m!} = \mathbb{1} + A + \frac{A^2}{2} + \dots, \quad (8.4)$$

which calls for a quadratic matrix A and therefore $N_1 = N_2 = N$ and it makes sense to set $L_1 = L_2 = L$ to achieve a uniform spatial resolution. Note, that this series is not due to the time stepping, which is outsourced to the same exact operator splitting as before.

The potential evolution operator includes a matrix exponential as well, but due to the time dependence has to be computed every time step:

$$\hat{U}_V = \exp\{-iaV(|\psi(x_{\mathbf{n}})|)^2\}. \quad (8.5)$$

A question that arises is to which accuracy the matrix exponentials of Eq. (8.3) and (8.5) have to be calculated. We can not expect either of $V(|\psi|^2)$ or $k_{\mathbf{n}}$ to be nilpotent: $A^m = 0 \quad \forall m > m_0$ would truncate Eq. (8.4) to a finite series. More effective is diagonalizing those matrices with a change-of-basis matrix S , such that the eigenvalues are on the diagonal:

$$\exp\{A\} = S \text{diag}[e^{\lambda_1}, \dots, e^{\lambda_N}] S^{-1}. \quad (8.6)$$

What has been omitted so far, is the calculation of the potential. Also the kernel coefficient matrix is not diagonal as before, Eq. (4.8), and Eq. (4.9) turns into a matrix-matrix multiplication:

$$V(|\psi(x_{\mathbf{n}})|^2) = \mathcal{F}^{-1} \hat{\mathbf{U}} \mathcal{F} |\psi(x_{\mathbf{n}})|^2 \quad \text{with} \quad \hat{\mathbf{U}} = \left[-\frac{1}{k_{\mathbf{n}}^2} \right]. \quad (8.7)$$

Performing a discrete Fourier transform needs one summation more than before, but the general procedure stays the same:

$$\begin{aligned} \psi(k_{\mathbf{n}}) &= \sum_{\mathbf{n}>0} \psi(x_{\mathbf{n}}) e^{-ik_{\mathbf{n}}x_{\mathbf{n}}} \\ &= \sum_{\mathbf{n}_2>0} \sum_{\mathbf{n}_1>0} e^{-ik_{\mathbf{n}_2}x_2} e^{-ik_{\mathbf{n}_1}x_1} \psi(x_{\mathbf{n}}). \end{aligned} \quad (8.8)$$

Part I

Appendix

A Additional Figures

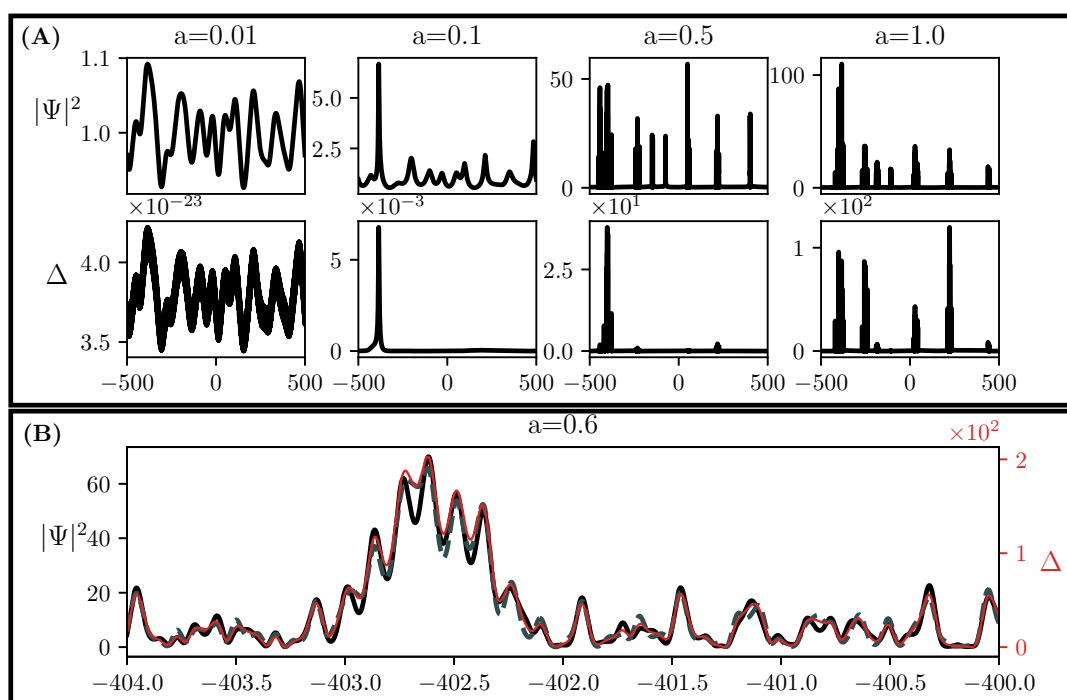


Figure A.1: (A): Wave function in a large box ($L=1000$) of the B-spline as well as the Fourier method and their difference Δ at various stages of the integration given in terms of the scale factor a . Differences between the solutions are limited by numerical precision in the beginning of the simulation and grow to $\mathcal{O}(1)$ already before the simulation end. (B): Zoom into the black box at $a = 0.6$. Differences in the two methods are still approximately proportional to the density itself.

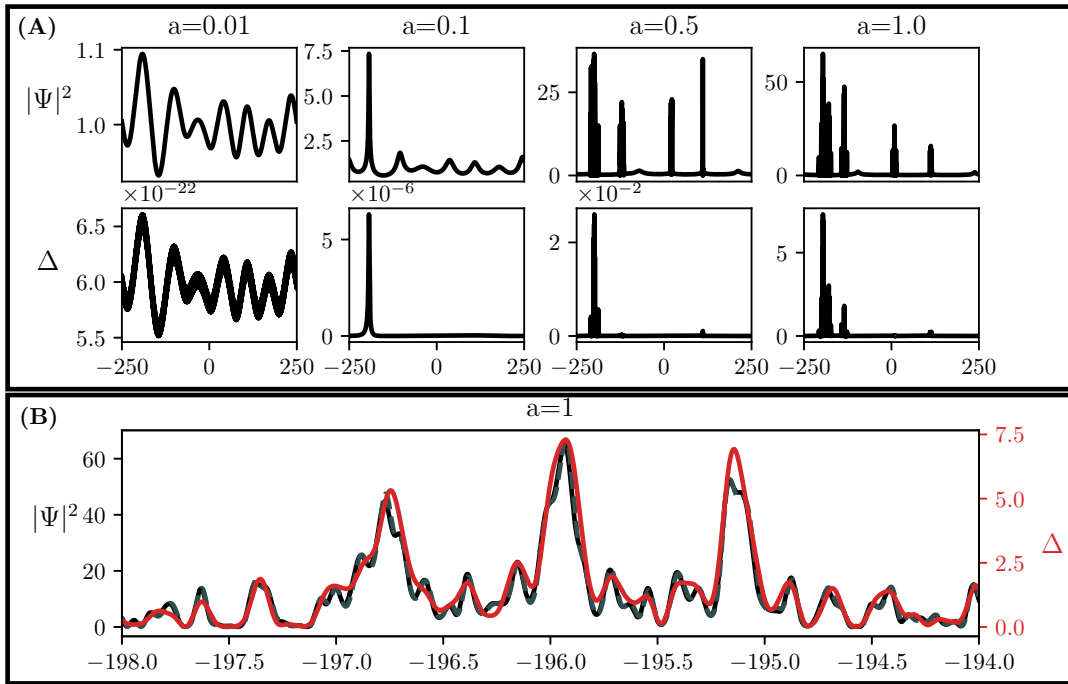


Figure A.2: (A): Wave function in a medium sized box ($L=500$) of the B-spline as well as the Fourier method and their difference Δ at various stages of the integration given in terms of the scale factor a . Differences between the solutions are limited by numerical precision in the beginning of the simulation and grow to $\mathcal{O}(10\%)$ at the simulation end. (B): Zoom into the black box at $a = 1$. Differences in the two methods are approximately proportional to the density itself.

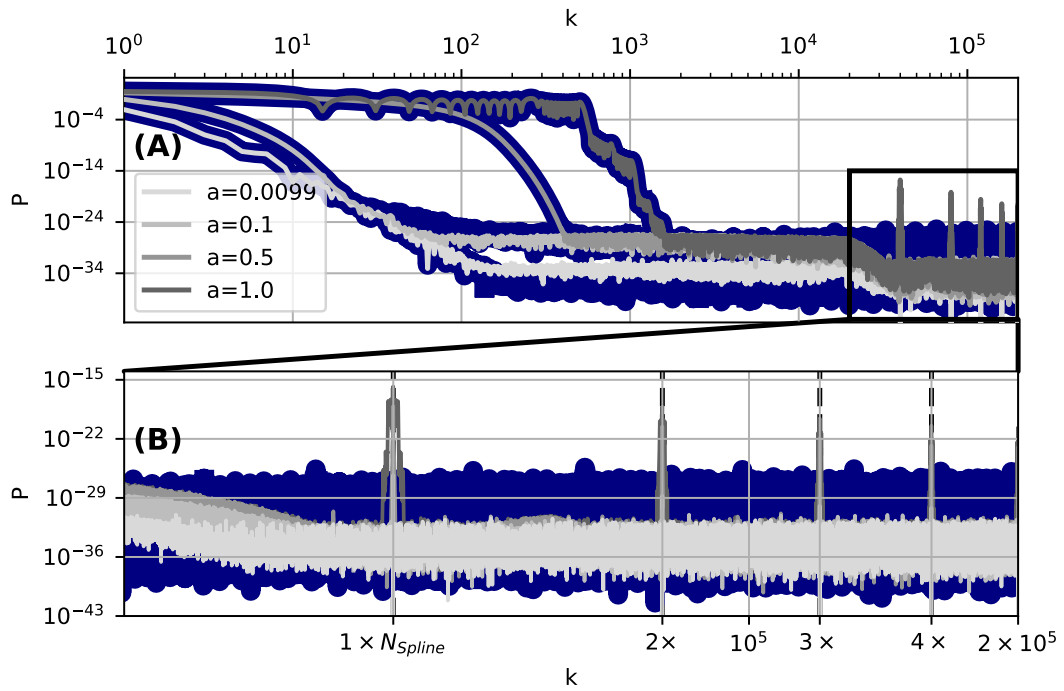


Figure A.3: (A): Evolution of the power spectra in the small box ($L = 100$) in terms of the scale factor a . The Fourier basis method (blue) underlies the B-splines in grey color. Modes $k < N_{Spline}/2$ coincide in their spectra. (B): Zoom-in of the 'oversampled' B-Splines. Peaks show up at multiples of the grid size at $k = nN_{Spline}$, $n \in \mathbb{N}$ (black dashed lines). They exist early on and expand during integration.

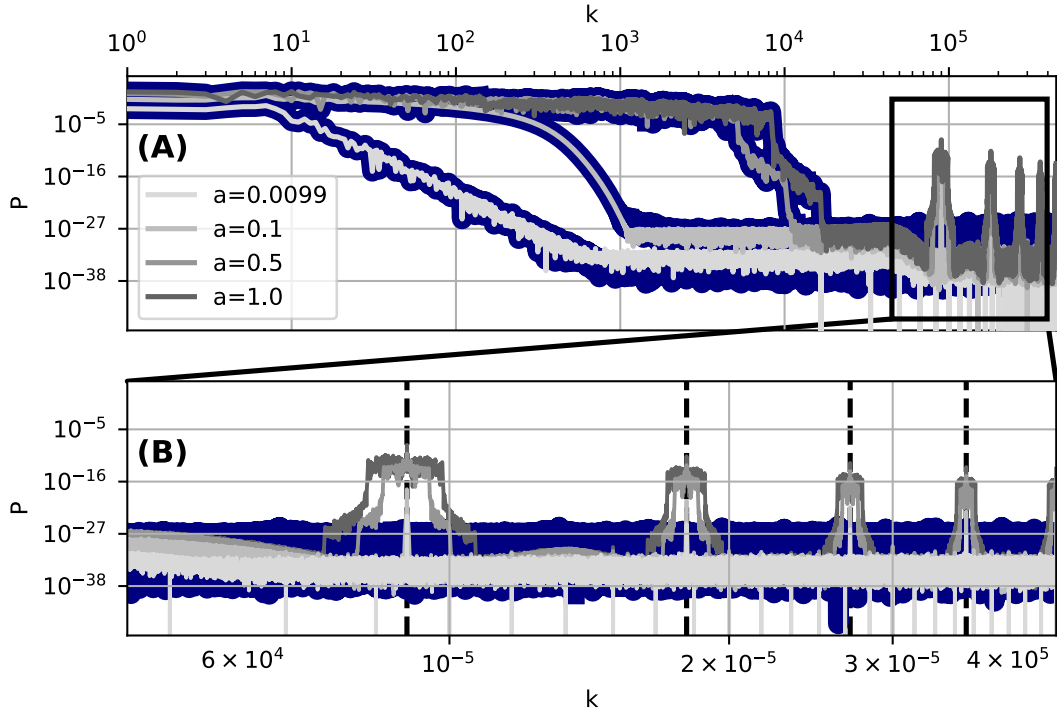


Figure A.4: (A): Evolution of the power spectra in the medium sized box ($L = 500$) in terms of the scale factor a . The Fourier basis method (blue) underlies the B-splines in grey color. Modes $k < N_{Spline}/2$ coincide in their spectra. (B): Zoom-in of the 'oversampled' B-Splines. Peaks show up at multiples of the grid size at $k = nN_{spline}$, $n \in \mathbb{N}$ (black dashed lines). They exist early on and expand during integration.

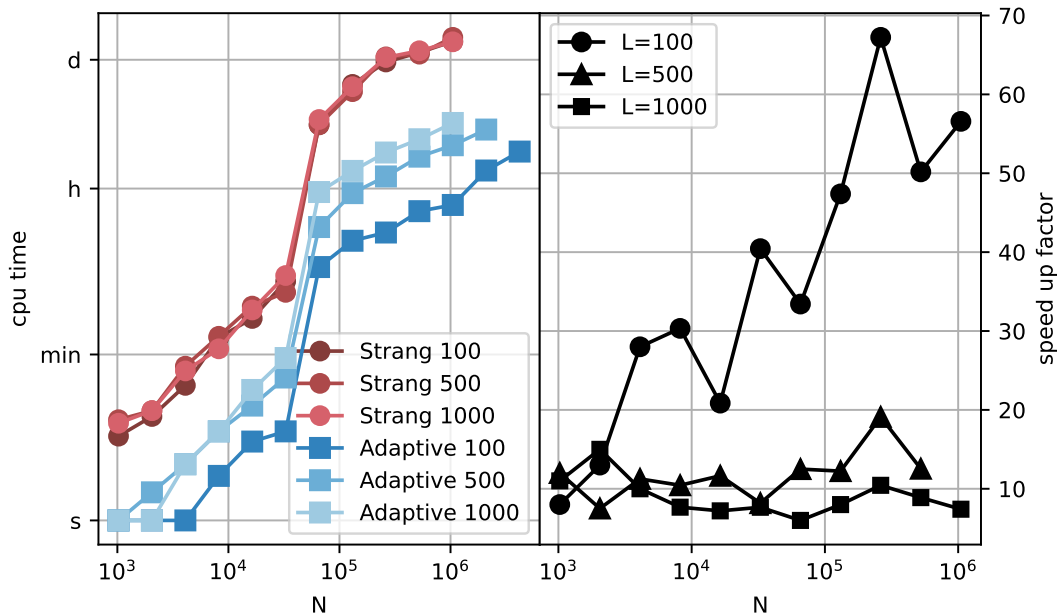


Figure A.5: Cpu usage and speed up factor of the three boxes sizes $L \in \{100, 500, 1000\}$. Tolerance parameters are chosen identical ($tol = 10^{-3}$), which leads to high accuracy solutions for larger boxes. Speed up factors are $\mathcal{O}(10)$.

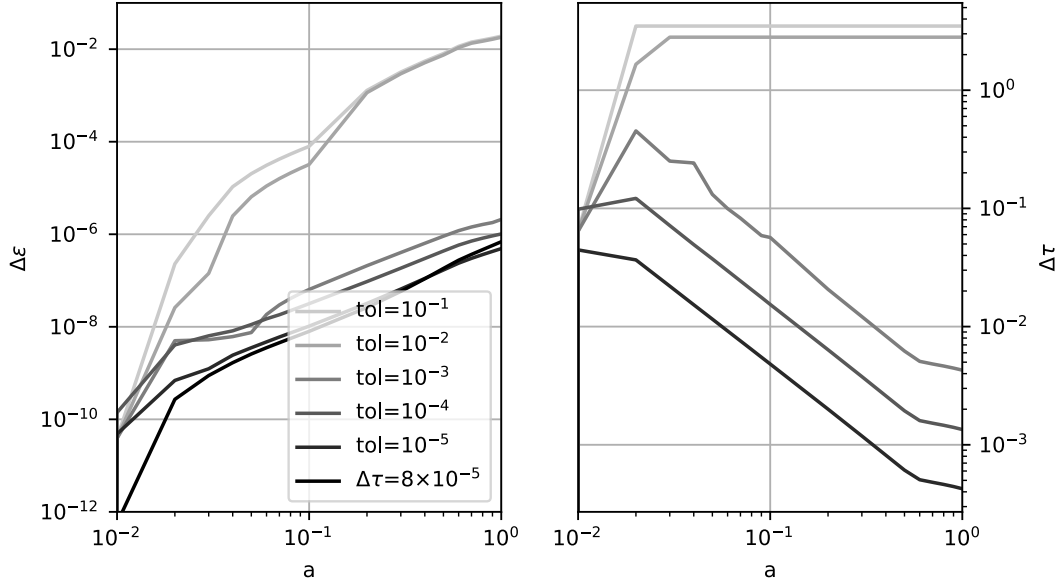


Figure A.6: Left: Deviation from the reference solution as a function of the scale factor (time) in the $L = 100$ box. Five adaptive, 4th order solutions with different tol parameters are shown. One converged, second order solution with a constant time step $\Delta\tau = 8 \times 10^{-5}$ marks the fidelity limit of the reference solution. Right: Evolution of the time step $\Delta\tau$ during integration. With $tol \leq 10^{-3}$ the time step $\Delta\tau$ stays below 1 and errors are small. $\Delta\tau$ grows beyond 1, where the adaptive time step selection does no longer work. Errors consequently grow rapidly.

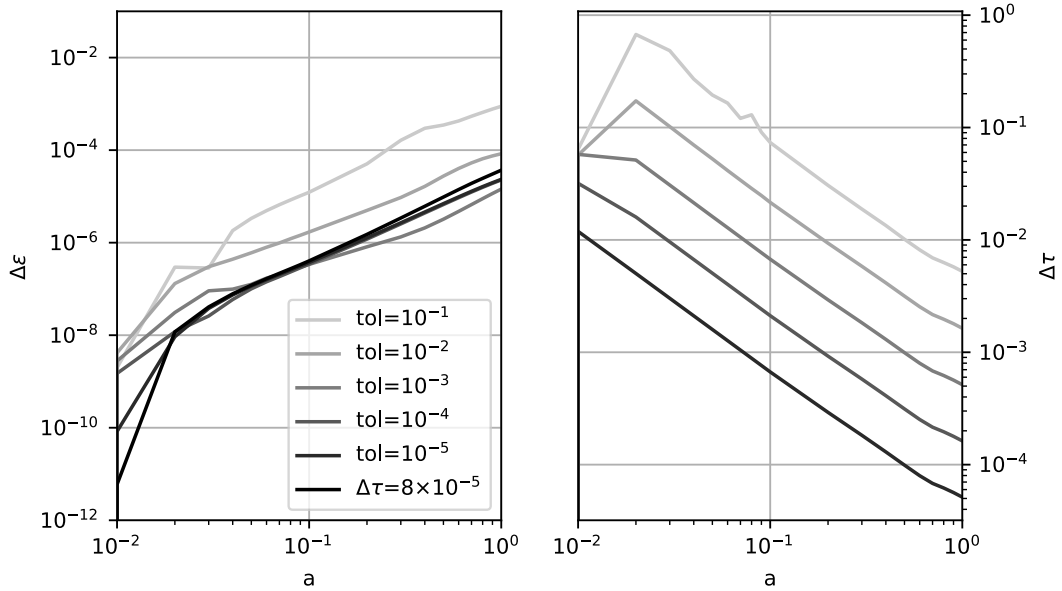


Figure A.7: Left: Deviation from the reference solution as a function of the scale factor (time) in the $L = 1000$ box. Five adaptive, 4th order solutions with different tol parameters are shown and one converged second order solution with a constant time step $\Delta\tau$. Right: Evolution of the time step $\Delta\tau$ during integration. Here, time step selection works well for $tol \leq 10^{-1}$.

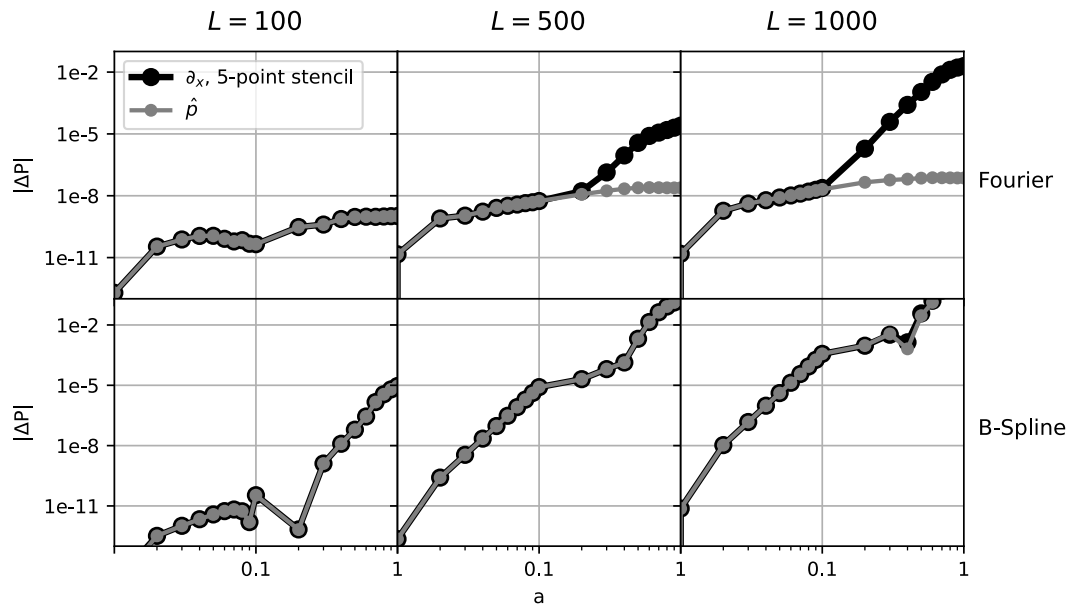


Figure A.8: Momentum conservation of the Fourier and B-Spline method for the tree box sizes. The momentum is calculated in two ways - the finite differencing 5-point stencil and a direct application of the momentum operator in k-space.

B Lists

B.1 List of Figures

2.1	Interaction kernels of the two dimension-reduced models. Blue: (1 + 1)-SP; shades of red: PLAM. Mind the different scaling of the x -axis between left and right. As a reference, the same three dimensional kernel is shown in the black, dashed line on both, the left and right side. Figure taken from Zimmermann et al. [2021] ; copyright: APS	14
3.1	Scale factor a as a function of the dimensionless time τ obtained from numerical integration. Small matter density parameters $\Omega_{m,0}$ result in slower growing universes.	18
3.2	Exemplary, rescaled cosmological initial states scaled with the box size L for a better comparison. Dimensionless box sizes $L \in \{48, \dots, 4877\}$ correspond to real distances of $L \in \{1 \text{ Mpc}, \dots, 100 \text{ Mpc}\}$. The finite correlation length σ together with the periodic box suppresses the structure in small boxes. Density fluctuations grow in amplitude and in their number of oscillations as the box size increases. They saturate at $\delta \approx 0.15$	21
5.1	Convergence behavior with respect to different parameters in (1+1)-SP. Each cell colour-maps the errors $\Delta\epsilon$ with respect to the black-square reference. Three box sizes $L \in 100, 500, 1000$ are plotted row-wise. The time development is given column-wise in terms of the scale factor a . The N -grid is in powers of 2, due to the FFT algorithm. To make it easier to read, N and $\Delta\tau$ have ticks at powers of 10. Errors induced by constraints in Δx show in a sharp edge in N -direction, which moves toward higher N as the non-linearity increases. Issues in the time domain on the contrary create a smooth saturation with decreasing $\Delta\tau$, that does not move with time.	27
5.2	Convergence behavior with respect to different parameters under strong confinement ($\sigma = 0.01$). All remaining parameters are as in Fig. 5.1. In comparison to (1+1)-SP errors stay three order of magnitude smaller. With respect to the space constraints, the confinement model is a lot less demanding and even $N \approx 1000$ basis functions are sufficient to resolve all features. In the time domain we see the same smooth saturation toward decreasing $\Delta\tau$	28
5.3	Evolution of small modes k_n of the power spectrum normalized with the linear theory, Eq. (5.3). 20 runs with varied initial states are averaged. The smallest modes show good agreement at early times until they decouple at late times.	30

- 5.4 Total cpu time and memory requirements as a function of the basis size. The expected scaling functions are fitted. A time step $\Delta\tau = 10^{-2}$ was used, which allows computing large basis sizes within reasonable time. For smaller $\Delta\tau$ these plots have to be rescaled with a constant factor. Small basis simulations are more efficient, as long as important vectors fit into the processors cache (SRAM). Runs with middle sized N scale worse, because the limiting factor is memory access. At large N Fourier transforms take the most time and the scaling is as expected $\propto N\log N$. 31
- 6.1 Densities at various stages of the minimization procedure with $a = 1$ and ground state mass $M = 100$. (A): The $(1 + 1)$ -SP ground state is reached quickly. (B): In PLAM ($\epsilon = 10^{-2}$) the imaginary time propagation takes longer. Note how the confinement manifests in the size of the ground state. 34
- 6.2 Inelastic interaction of an asymmetric high-mass, low-mass ground state configuration under strong, transversal confinement ($\epsilon = 10^{-2}$) and $a = 1$. The evolution starts from (6.2). Panel (A): Density evolution. Initially, both densities travel as solitary waves (red), pass through each other (black, inset) and continue to propagate in a quasi-solitary movement after the interaction (orange). By this we mean a state for which neither linear dispersive nor nonlinear focusing effects induce a permanent deformation of the density. Instead, one observes an oscillation around a solitary wave. Similar oscillatory behavior was found for $(3 + 1)$ -SP, [Guzmán and Ureña-López \[2004\]](#), once the ground state density is perturbed. Panel (B): Time evolution of the mass deviation of both ground states relative to their initial masses cf. Eq. (6.3). Post-interaction, it is the high-mass ground state gaining additional matter at the expense of the lighter ground state. Panel (C): Time evolution of the total energy deviation of both ground states relative to their respective initial total energies. As for the mass, the interaction induces an energy transfer from the low to high mass ground state. Notice, how the quasi-solitary behavior of the post-interaction densities is also seen in an oscillation of the energy deviation. Since the association of mass and energy contained in the positive and negative box half to a particular solitary wave is ambiguous during the interaction, we deem data in the gray shaded interval of panel (B) and (C) as not reliable. Figure taken from [Zimmermann et al. \[2021\]](#); copyright APS 37

6.3	<p>Overview of asymptotic states as a function of the confinement parameter ϵ. From left to right, we have (A)-(B) analyzing the strong confinement limit ($\epsilon = 10^{-2}$), (C)-(D) assessing the weak confinement regime ($\epsilon = 5$) and (E)-(F) evaluating the uniform reduction scenario in the limit $\epsilon \rightarrow \infty$, i.e. (1 + 1)-SP. Upper panels: Snapshot of the attained quasi-stationary states. Lower panels: Comparison of the interaction range $R(L_3)$, (2.29), and the soliton size $\sigma(M)$, Eq. (6.4). Crosses denote soliton sizes directly inferred from the gradient descent of various mass solitons. Solitons with sizes inside the gray shaded area do not exist as they violate periodic boundary conditions. For $\epsilon > 1$, we find a transition away from turbulent soliton dynamics toward a "incoherent soliton" configuration, i.e. a highly fluctuating state comprised of many density maxima beating against each other in real space. As argued in Picozzi and Garnier [2011], this regime is entered once the interaction range $R(L_3)$ is significantly larger than the soliton size $\sigma(M)$. Even in the best case scenario for (D) and (F), i.e. when a soliton of maximal size could form, one still finds $\sigma_{\max}/R(L_3 \approx 127) < 0.1$ — far outside the soliton regime. By contrast, the strong confinement scenario of (A) realizes $\sigma(M = 48)/R(L_3 \approx 127) > 1$ and is therefore well inside the soliton regime. Figure taken from Zimmermann et al. [2021]; copyright APS</p>	39
7.1	<p>(A): Wave function in a small box ($L=100$) of the B-spline as well as the Fourier method and their difference Δ at various stages of the integration given in terms of the scale factor a. Differences between the solutions are limited by numerical precision in the beginning of the simulation and grow to $\mathcal{O}(10^{-5})$ at the simulation end. (B): Zoom into the black box at $a = 1$. Differences in the two methods are approximately proportional to the density itself.</p>	42
7.2	<p>(A): Evolution of the power spectra in the large box ($L = 1000$) in terms of the scale factor a. The Fourier basis method (blue) underlies the B-splines in grey color. Modes $k < N_{\text{spline}}/2$ coincide in their spectra. (B): Zoom-in of the 'oversampled' B-Splines. Peaks show up at multiples of the grid size at $k = nN_{\text{spline}}$, $n \in \mathbb{N}$ (black dashed lines). They exist early on and expand during integration.</p>	43
7.3	<p>Convergence of the fourth order integrator relative to the same reference as in Fig. 5.1. The space domain behaves exactly as before. On contrast, the convergence is much faster with regards to the time step, such that the plateau is reached at $\Delta\tau \approx 5 \times 10^{-3}$.</p>	45
7.4	<p>Left: Deviation from the reference solution as a function of the scale factor (time) in the $L = 500$ box. Five adaptive, 4th order solutions with different tol parameters are shown and one converged second order solution with a constant time step $\Delta\tau$. Right: Evolution of the time step $\Delta\tau$ during integration. Here, time step selection works well for $tol \leq 10^{-2}$.</p>	47
7.5	<p>Cpu usage and speed up factor of the three boxes sizes $L \in \{100, 500, 1000\}$. Tolerance parameters are chosen as $tol \in \{10^{-3}, 10^{-2}, 10^{-1}\}$ - within the stability region, where $\Delta\tau \leq 1$. Remarkable speed up factors around 50 are possible.</p>	48

7.6	Conservation of mass of Fourier, B-Spline and the new adaptive method for three box sizes. The Fourier method conserves the total mass below the 10^{-6} range, whereas the B-spline method is in advantage for smaller L , but struggles with the larger boxes, where $ \Delta M $ grows to $\mathcal{O}(10^{-3})$. The adaptive method is the most advanced solution. It starts at $ \Delta M = \mathcal{O}(10^{-12})$ and stays bounded by $ \Delta M = \mathcal{O}(10^{-9})$	50
7.7	Momentum conservation of the Fourier, B-Spline and the new adaptive method for the three box sizes. The momentum is calculated in k-space directly by application of the momentum operator. The situation is qualitatively similar to Fig. 7.6, but problems in the B-Spline method arise earlier than in the conservation of mass, because the momentum is a derived quantity.	51
7.8	Number of FFTs for the standard Strang splitting and the adaptive method, which has $\mathcal{O}(10^3)$ less FFTs. Also, #FFTs grows significantly, even at late times, in the case of time adaptivity.	51
A.1	(A): Wave function in a large box ($L=1000$) of the B-spline as well as the Fourier method and their difference Δ at various stages of the integration given in terms of the scale factor a . Differences between the solutions are limited by numerical precision in the beginning of the simulation and grow to $\mathcal{O}(1)$ already before the simulation end. (B): Zoom into the black box at $a = 0.6$. Differences in the two methods are still approximately proportional to the density itself.	57
A.2	(A): Wave function in a medium sized box ($L=500$) of the B-spline as well as the Fourier method and their difference Δ at various stages of the integration given in terms of the scale factor a . Differences between the solutions are limited by numerical precision in the beginning of the simulation and grow to $\mathcal{O}(10\%)$ at the simulation end. (B): Zoom into the black box at $a = 1$. Differences in the two methods are approximately proportional to the density itself.	58
A.3	(A): Evolution of the power spectra in the small box ($L = 100$) in terms of the scale factor a . The Fourier basis method (blue) underlies the B-splines in grey color. Modes $k < N_{Spline}/2$ coincide in their spectra. (B): Zoom-in of the 'oversampled' B-Splines. Peaks show up at multiples of the grid size at $k = nN_{Spline}$, $n \in \mathbb{N}$ (black dashed lines). They exist early on and expand during integration.	59
A.4	(A): Evolution of the power spectra in the medium sized box ($L = 500$) in terms of the scale factor a . The Fourier basis method (blue) underlies the B-splines in grey color. Modes $k < N_{Spline}/2$ coincide in their spectra. (B): Zoom-in of the 'oversampled' B-Splines. Peaks show up at multiples of the grid size at $k = nN_{Spline}$, $n \in \mathbb{N}$ (black dashed lines). They exist early on and expand during integration.	60
A.5	Cpu usage and speed up factor of the three boxes sizes $L \in \{100, 500, 1000\}$. Tolerance parameters are chosen identical ($tol = 10^{-3}$	60

A.6	Left: Deviation from the reference solution as a function of the scale factor (time) in the $L = 100$ box. Five adaptive, 4th order solutions with different tol parameters are shown. One converged, second order solution with a constant time step $\Delta\tau = 8 \times 10^{-5}$ marks the fidelity limit of the reference solution. Right: Evolution of the time step $\Delta\tau$ during integration. With $tol \leq 10^{-3}$ the time step $\Delta\tau$ stays below 1 and errors are small. $\Delta\tau$ grows beyond 1, where the adaptive time step selection does no longer work. Errors consequently grow rapidly.	61
A.7	Left: Deviation from the reference solution as a function of the scale factor (time) in the $L = 1000$ box. Five adaptive, 4th order solutions with different tol parameters are shown and one converged second order solution with a constant time step $\Delta\tau$. Right: Evolution of the time step $\Delta\tau$ during integration. Here, time step selection works well for $tol \leq 10^{-1}$	61
A.8	Momentum conservation of the Fourier and B-Spline method for the tree box sizes. The momentum is calculated in two ways - the finite differencing 5-point stencil and a direct application of the momentum operator in k-space.	62

B.2 List of Tables

2.1	Variables and abbreviations	9
4.1	Existing codes to simulate Dark Matter adapted from Zhang et al. [2019] . More recent developments were added. Quantitative features stem from the respective publications. The first half are Schrödinger-Poisson solvers, the second half hydrodynamic solvers.	22

C Bibliography

- Luca Amendola. Lecture notes: Cosmology, 2022. URL <https://www.thphys.uni-heidelberg.de/~amendola/teaching/cosmology.pdf>.
- Winfried Auzinger. Coefficients of various splitting methods, 2021. URL <https://www.asc.tuwien.ac.at/~winfried/splitting/index.php?rc=0&ab=bm116-prk-ab&name=BM%2011-6%20PRK>.
- Winfried Auzinger, Harald Hofstätter, David Ketcheson, and Othmar Koch. Practical splitting methods for the adaptive integration of nonlinear evolution equations. part i: Construction of optimized schemes and pairs of schemes. *BIT Numerical Mathematics*, 57, 04 2016a. doi: 10.1007/s10543-016-0626-9.
- Winfried Auzinger, Othmar Koch, and Michael Quell. Adaptive high-order splitting methods for systems of nonlinear evolution equations with periodic boundary conditions, 2016b.
- H Bachau, E Cormier, P Decleva, J E Hansen, and F Martín. Applications of B-splines in atomic and molecular physics. *Reports on Progress in Physics*, 64(12):1815–1943, nov 2001. doi: 10.1088/0034-4885/64/12/205. URL <https://doi.org/10.1088/0034-4885/64/12/205>.
- Weizhu Bao, I-Liang Chern, and Fong Lim. Efficient and spectrally accurate numerical methods for computing ground and first excited states in bose–einstein condensates. *Journal of Computational Physics*, 219:836–854, 12 2006. doi: 10.1016/j.jcp.2006.04.019.
- Matthias Bartelmann. Gravitational lensing. *Classical and Quantum Gravity*, 27(23): 233001, Nov 2010. ISSN 1361-6382. doi: 10.1088/0264-9381/27/23/233001. URL <http://dx.doi.org/10.1088/0264-9381/27/23/233001>.
- James Binney. Discreteness effects in cosmological N-body simulations. *Monthly Notices of the Royal Astronomical Society*, 350(3):939–948, May 2004. doi: 10.1111/j.1365-2966.2004.07699.x.
- Greg L. Bryan, Michael L. Norman, Brian W. O’Shea, Tom Abel, John H. Wise, Matthew J. Turk, Daniel R. Reynolds, David C. Collins, Peng Wang, Samuel W. Skillman, Britton Smith, Robert P. Harkness, James Bordner, Ji hoon Kim, Michael Kuhlen, Hao Xu, Nathan Goldbaum, Cameron Hummels, Alexei G. Kritsuk, Elizabeth Tasker, Stephen Skory, Christine M. Simpson, Oliver Hahn, Jeffrey S. Oishi, Geoffrey C. So, Fen Zhao, Renyue Cen, and Yuan Li and. ENZO: AN ADAPTIVE MESH REFINEMENT CODE FOR ASTROPHYSICS. *The Astrophysical Journal Supplement Series*, 211(2):19, mar 2014a. doi: 10.1088/0067-0049/211/2/19. URL <https://doi.org/10.1088/0067-0049/211/2/19>.

- Greg L. Bryan, Michael L. Norman, Brian W. O'Shea, Tom Abel, John H. Wise, Matthew J. Turk, Daniel R. Reynolds, David C. Collins, Peng Wang, Samuel W. Skillman, and et al. Enzo: An adaptive mesh refinement code for astrophysics. *The Astrophysical Journal Supplement Series*, 211(2):19, Mar 2014b. ISSN 1538-4365. doi: 10.1088/0067-0049/211/2/19. URL <http://dx.doi.org/10.1088/0067-0049/211/2/19>.
- Philippe Choquard, Joachim Stubbe, and Marc Vuffray. Stationary solutions of the schrödinger-newton model - an ode approach. *Differential and Integral Equations*, 21, 01 2008.
- Álefe de Almeida, Luca Amendola, and Viviana Niro. Galaxy rotation curves in modified gravity models. *Journal of Cosmology and Astroparticle Physics*, 2018(08): 012–012, Aug 2018. ISSN 1475-7516. doi: 10.1088/1475-7516/2018/08/012. URL <http://dx.doi.org/10.1088/1475-7516/2018/08/012>.
- Antonino Del Popolo and Morgan Le Delliou. Review of solutions to the cusp-core problem of the Λ cdm model. *Galaxies*, 9(4), 2021. ISSN 2075-4434. URL <https://www.mdpi.com/2075-4434/9/4/123>.
- Scott Dodelson. *Modern cosmology*. Academic Press, 2003.
- P. G. Drazin. *Solitons: an introduction*. Cambridge University Press, Cambridge England New York, 1989. ISBN 9781139172059.
- Mathias Garny, Thomas Konstandin, and Henrique Rubira. The schrödinger-poisson method for large-scale structure. *Journal of Cosmology and Astroparticle Physics*, 2020 (04):003–003, Apr 2020. ISSN 1475-7516. doi: 10.1088/1475-7516/2020/04/003. URL <http://dx.doi.org/10.1088/1475-7516/2020/04/003>.
- Andrew S. Goetz. The einstein-klein-gordon equations, wave dark matter, and the tully-fisher relation, 2015.
- I.S. Gradshteyn and I.M. Ryzhik. Table of integrals, series and products, 2007. URL <http://fisica.ciens.ucv.ve/~svincenz/TISPISGIMR.pdf>.
- F. Siddhartha Guzmán and L. Arturo Ureña-López. Evolution of the Schrödinger-Newton system for a self-gravitating scalar field. *Physical Review D*, 69(12), June 2004. doi: 10.1103/physrevd.69.124033.
- R. E. Hunt. Lecture notes of mathematical methods ii, chapter 2: Poisson's equation, 2002. URL <https://www.damtp.cam.ac.uk/user/reh10/lectures/nst-mmii-chapter2.pdf>.
- Jonathan Klos. Bachelor thesis, 2018. URL https://www.thphys.uni-heidelberg.de/~wimberger/ba_klos.pdf.
- Xinyu Li, Lam Hui, and Greg L. Bryan. Numerical and perturbative computations of the fuzzy dark matter model. *Physical Review D*, 99(6), Mar 2019. ISSN 2470-0029. doi: 10.1103/physrevd.99.063509. URL <http://dx.doi.org/10.1103/PhysRevD.99.063509>.

- D. Lynden-Bell. Statistical Mechanics of Violent Relaxation in Stellar Systems. *Monthly Notices of the Royal Astronomical Society*, 136(1):101–121, May 1967. doi: 10.1093/mnras/136.1.101.
- Simon L Marshall. A periodic green function for calculation of coulombic lattice potentials. *Journal of Physics: Condensed Matter*, 12(21):4575–4601, may 2000. doi: 10.1088/0953-8984/12/21/304. URL <https://doi.org/10.1088/0953-8984/12/21/304>.
- Gradimir V. Milovanović and Zlatko Udovičić. Calculation of coefficients of a cardinal b-spline. *Applied Mathematics Letters*, 23(11):1346–1350, 2010. ISSN 0893-9659. doi: <https://doi.org/10.1016/j.aml.2010.06.029>. URL <https://www.sciencedirect.com/science/article/pii/S0893965910002284>.
- Mattia Mina, David F. Mota, and Hans A. Winther. Scalar: an amr code to simulate axion-like dark matter models. *Astronomy & Astrophysics*, 641:A107, Sep 2020. ISSN 1432-0746. doi: 10.1051/0004-6361/201936272. URL <http://dx.doi.org/10.1051/0004-6361/201936272>.
- Jens Niemeyer. Small-scale structure of fuzzy and axion-like dark matter. *Progress in Particle and Nuclear Physics*, 113:103787, 04 2020. doi: 10.1016/j.ppnp.2020.103787.
- Tao Pang. *An Introduction to Computational Physics*. Cambridge University Press, 2006. doi: 10.1017/cbo9780511800870.
- Antonio Picozzi and Josselin Garnier. Incoherent Soliton Turbulence in Nonlocal Nonlinear Media. *Physical Review Letters*, 107(23), November 2011. doi: 10.1103/physrevlett.107.233901.
- A. Ratnani and E. Sonnenndrucker. B-splines and isogeometric analysis, 2016. URL https://www-m16.ma.tum.de/foswiki/pub/M16/Allgemeines/AdvFE16/bsplines_Ahmed.pdf.
- Keir K. Rogers and Hiranya V. Peiris. Strong bound on canonical ultralight axion dark matter from the lyman-alpha forest. *Physical Review Letters*, 126(7), Feb 2021. ISSN 1079-7114. doi: 10.1103/physrevlett.126.071302. URL <http://dx.doi.org/10.1103/PhysRevLett.126.071302>.
- Tanya S. Roussy, Daniel A. Palken, William B. Cairncross, Benjamin M. Brubaker, Daniel N. Gresh, Matt Grau, Kevin C. Cossel, Kia Boon Ng, Yuval Shagam, Yan Zhou, Victor V. Flambaum, Konrad W. Lehnert, Jun Ye, and Eric A. Cornell. Experimental constraint on axionlike particles over seven orders of magnitude in mass. *Physical Review Letters*, 126(17), Apr 2021. ISSN 1079-7114. doi: 10.1103/physrevlett.126.171301. URL <http://dx.doi.org/10.1103/PhysRevLett.126.171301>.
- Barbara Sue Ryden. *Introduction to Cosmology*. Addison-Wesley, 2003.
- Borna Salehian, Hong-Yi Zhang, Mustafa A. Amin, David I. Kaiser, and Mohammad Hossein Namjoo. Beyond schrödinger-poisson: nonrelativistic effective field theory for scalar dark matter. *Journal of High Energy Physics*, 2021(9), Sep 2021. ISSN 1029-8479. doi: 10.1007/jhep09(2021)050. URL [http://dx.doi.org/10.1007/JHEP09\(2021\)050](http://dx.doi.org/10.1007/JHEP09(2021)050).

- Hsi-Yu Schive, Tzihong Chiueh, and Tom Broadhurst. Cosmic structure as the quantum interference of a coherent dark wave. *Nature Physics*, 10(7):496–499, Jun 2014. ISSN 1745-2481. doi: 10.1038/nphys2996. URL <http://dx.doi.org/10.1038/nphys2996>.
- Hsi-Yu Schive, John A ZuHone, Nathan J Goldbaum, Matthew J Turk, Massimo Gaspari, and Chin-Yu Cheng. gamer-2: a gpu-accelerated adaptive mesh refinement code – accuracy, performance, and scalability. *Monthly Notices of the Royal Astronomical Society*, 481(4):4815–4840, Sep 2018a. ISSN 1365-2966. doi: 10.1093/mnras/sty2586. URL <http://dx.doi.org/10.1093/mnras/sty2586>.
- Hsi-Yu Schive, John A ZuHone, Nathan J Goldbaum, Matthew J Turk, Massimo Gaspari, and Chin-Yu Cheng. gamer-2: a gpu-accelerated adaptive mesh refinement code – accuracy, performance, and scalability. *Monthly Notices of the Royal Astronomical Society*, 481(4):4815–4840, Sep 2018b. ISSN 1365-2966. doi: 10.1093/mnras/sty2586. URL <http://dx.doi.org/10.1093/mnras/sty2586>.
- Edward Seidel and Wai-Mo Suen. Formation of solitonic stars through gravitational cooling. *Physical Review Letters*, 72(16):2516–2519, April 1994. doi: 10.1103/physrevlett.72.2516.
- Thierry Sousbie and Stéphane Colombi. Coldice: A parallel vlasov–poisson solver using moving adaptive simplicial tessellation. *Journal of Computational Physics*, 321: 644–697, Sep 2016. ISSN 0021-9991. doi: 10.1016/j.jcp.2016.05.048. URL <http://dx.doi.org/10.1016/j.jcp.2016.05.048>.
- Volker Springel, Rüdiger Pakmor, Oliver Zier, and Martin Reinecke. Simulating cosmic structure formation with the gadget-4 code. *Monthly Notices of the Royal Astronomical Society*, Jul 2021. ISSN 1365-2966. doi: 10.1093/mnras/stab1855. URL <http://dx.doi.org/10.1093/mnras/stab1855>.
- Atsushi Taruya and Stéphane Colombi. Post-collapse perturbation theory in 1d cosmology – beyond shell-crossing. *Monthly Notices of the Royal Astronomical Society*, 470(4):4858–4884, Jun 2017. ISSN 1365-2966. doi: 10.1093/mnras/stx1501. URL <http://dx.doi.org/10.1093/mnras/stx1501>.
- R. Teyssier. Cosmological hydrodynamics with adaptive mesh refinement. A new high resolution code called RAMSES. *AAP*, 385:337–364, April 2002. doi: 10.1051/0004-6361:20011817.
- Michael S. Turner. Λ cdm: Much more than we expected, but now less than what we want. 2021.
- Jan Veltmaat, Jens C. Niemeyer, and Bodo Schwabe. Formation and structure of ultralight bosonic dark matter halos. *Phys. Rev. D*, 98:043509, Aug 2018. doi: 10.1103/PhysRevD.98.043509. URL <https://link.aps.org/doi/10.1103/PhysRevD.98.043509>.
- Timothy C. Wallstrom. Inequivalence between the schrödinger equation and the madelung hydrodynamic equations. *Phys. Rev. A*, 49:1613–1617, Mar 1994. doi: 10.1103/PhysRevA.49.1613. URL <https://link.aps.org/doi/10.1103/PhysRevA.49.1613>.

- Sandro Wimberger, Riccardo Mannella, Oliver Morsch, and Ennio Arimondo. Resonant Nonlinear Quantum Transport for a Periodically Kicked Bose Condensate. *Phys. Rev. Lett.*, 94:130404, April 2005. doi: 10.1103/PhysRevLett.94.130404. URL <https://link.aps.org/doi/10.1103/PhysRevLett.94.130404>.
- Jiajun Zhang, Hantao Liu, and Ming-Chung Chu. Cosmological simulation for fuzzy dark matter model. *Frontiers in Astronomy and Space Sciences*, 5, 01 2019. doi: 10.3389/fspas.2018.00048.
- Tim Zimmermann. An investigation of the lower dimensional dynamics of fuzzy dark matter. Master's thesis, Universität Heidelberg, 2019.
- Tim Zimmermann, Massimo Pietroni, Javier Madroñero, Luca Amendola, and Sandro Wimberger. A quantum model for the dynamics of cold dark matter. *Condensed Matter*, 4:89, 11 2019. doi: 10.3390/condmat4040089.
- Tim Zimmermann, Nico Schwersenz, Massimo Pietroni, and Sandro Wimberger. One-dimensional fuzzy dark matter models: Structure growth and asymptotic dynamics. *Physical Review D*, 103(8), Apr 2021. ISSN 2470-0029. doi: 10.1103/physrevd.103.083018. URL <http://dx.doi.org/10.1103/PhysRevD.103.083018>.

Acknowledgement

The author acknowledges support by the state of Baden-Württemberg through bwHPC.

I would like to thank Luca Amendola and Massimo Pietroni for their input on cosmological topics. Thanks a lot, Javier Madroñero and Victor Loiza for your work on numerically related issues and the ease of our collaboration. I am especially grateful to Tim Zimmermann. You introduced me to this field of research and were always patient with me. Sandro Wimberger deserves my appreciation not only for the warm reception in Parma, but also for the continuous support throughout the last year, despite the wild conditions.

Erklärung

Ich versichere, dass ich diese Arbeit selbstständig verfasst habe und keine anderen als die angegebenen Quellen und Hilfsmittel benutzt habe.

Heidelberg, den 18.02.2022

Nico Schwesig
.....